THE PION DOUBLE CHARGE EXCHANGE REACTION ON ^{18}O AT 50 MeV.

by

NIGEL P. HESSEY

B.Sc. University of Nottingham, 1979

A THESIS SUBMITTED IN PARTIAL FULFILLMENT OF THE

REQUIREMENTS FOR THE DEGREE OF

MASTER OF SCIENCE

in

THE FACULTY OF GRADUATE STUDIES

Department of Physics

We accept this thesis as conforming

to the required standard

THE UNIVERSITY OF BRITISH COLUMBIA

September 1985

In presenting this thesis in partial fulfilment of the requirements for an advanced degree at the University of British Columbia, I agree that the Library shall make it freely available for reference and study. I further agree that permission for extensive copying of this thesis for scholarly purposes may be granted by the head of my department or by his or her representatives. It is understood that copying or publication of this thesis for financial gain shall not be allowed without my written permission.

Department of Physics

The University of British Columbia
1956 Main Mall
Vancouver, Canada
V6T 1Y3

Date 11th October 1985

ABSTRACT

This thesis discusses the pion double charge exchange (DCX) reaction $^{18}O(\pi^+,\pi^-)^{18}Ne$ at 50 MeV. Transitions to the ground state of ^{18}Ne, which is the double-isobaric-analogue state (DIAS) of ^{18}O, have been isolated. The differential cross sections for DIAS transitions have been measured at 6 scattering angles from 18.2° to 122.6°. The experiment was performed at TRIUMF in December 1984 using the QQD low energy pion spectrometer [26].

The differential cross section angular distribution is forward peaked, falling from 4.7±0.5 μb/sr at 0° (by extrapolation) to 0.61±0.11 μb/sr at 122.6°. The total (angle-integrated) cross section is 16.2±1.2 μb.

DCX measurements are expected to give information on nuclear structure that is hard to obtain by other reactions. This information includes short range correlations and neutron-proton density differences. However, before such information can be extracted the mechanism for DCX must be understood. The aim of this experiment was to provide more data to test the various theories of the DCX mechanisms. The implications of the results for several theories of DCX are discussed.

The forward peaking of DCX angular distributions at 50 MeV was unexpected. 50 MeV single charge exchange (SCX) angular distributions are forward dipped e.g. [14], a result of the cancellation of the 0° s and p wave scattering amplitudes for the reaction $p(\pi^+,\pi^\circ)n$. Early DCX calculations were based on the simple sequential mechanism. This assumes DCX proceeds via 2 successive SCX reactions, with the isobaric analogue as the intermediate state. These calculations predicted forward dipping and small cross sections for DCX [13,15]. The data shows this mechanism is an over-simplification.

The standard model for π-nucleus scattering is the optical potential. Johnson and Siciliano are developimg a potential with which to calculate

elastic, SCX and DCX cross sections [48,38,22]. They include second order terms, important in DCX because the reaction must involve scattering by at least two nucleons. By using a general form for the optical potential they include contributions from excited intermediate states.

Miller has suggested the forward peaking is due to the presence of six-quark clusters in the nucleus [16]. His model reproduces the data for 50 MeV DCX on ^{18}O and ^{14}C at forward angles.

Karapiperis and Kobayashi have used the Δ-hole model to calculate elastic, SCX and DCX cross sections [19]. They obtain fair agreement with data for a range of nuclei and energies.

Jennings et al. [22] are developing a model in which short range correlations produce the forward peaking. This work is at an early stage.

More DCX measurements are needed to choose between the various models. Measurements at 50 MeV are particularly valuable because the simple sequential mechanism is small, allowing other mechanisms to be observed. Further data such as excitation functions below 80 MeV and angular distributions for other nuclei are needed.

TABLE OF CONTENTS

LIST OF TABLES

LIST OF FIGURES

ACKNOWLEDGEMENTS

I would like to take this opportunity to thank all those who made this thesis possible, and made my time at TRIUMF so enjoyable. In particular I would like to thank Dick Johnson, my research supervisor, for his guidance; Ami Altman for so much help with the analysis; Uli Wienands for cross-checking the analysis; Dave Gill for his commitment to the QQD spectrometer; and to the rest of the PISCAT group who did so many shifts for data taking.

Finally, a very big thankyou to my wife Julie for typing and editing the thesis.

1 INTRODUCTION

This thesis describes an experiment to measure the pion double charge exchange (DCX) cross-section of ^{18}O, and discusses the results. The aim of the experiment was to obtain data that will help our understanding of the DCX mechanism.

1.1 Pions

Pions are the lightest mesons, with masses around 140 MeV. They are spinless, and they have three possible charge states, +1, -1 and 0. They are largely responsible for binding nucleons together in nuclei. The charged pions decay by the weak interaction with a mean-life of 2.60×10^{-8} s, the π° decays by the electromagnetic interaction with a mean-life of 0.9×10^{-16} s. Pions are produced at TRIUMF when protons with kinetic energy 500 MeV react with a production target. This allows beams of π^+ and π^- to be produced, whilst the π° decay too rapidly for beam production - at least at TRIUMF energies. For an introduction to pion-nucleus physics, see e.g. [1].

There are many reasons for using pions as nuclear probes. They interact with the nucleus via the strong interaction, whereas electrons interact via the electromagnetic interaction. So pions interact with neutrons as well as protons whereas electrons interact almost only with protons. Furthermore the π^+ reacts differently with a given type of nucleon - i.e. neutron or proton - to a π^-, due to isospin-space effects; so pions can probe differences between proton and neutron states [2,3,4].

1.2 Charge Exchange Reactions

Double charge-exchange (DCX) is one of many reactions pions have with nuclei. Experiments usually use π^+ beams; the π^+ gives up two units of

charge to the nucleus and emerges as a π^-. In the nucleus two neutrons are converted to two protons. The reaction $^{18}O(\pi^+,\pi^-)^{18}Ne$ is an example of pion double charge-exchange.

Pion single charge-exchange (SCX) is the related reaction in which the π^+ changes to a π°, and one neutron changes to a proton in the nucleus. SCX experiments look for the two gamma rays from the π° decay to signal an event.

The most studied DCX reactions are those in which the product nucleus is the double isobaric-analogue state (DIAS). For an isospin T=1, T_z=-1 nuclear state, the DIAS is the nuclear state with T=1, T_z=+1. For example, the DIAS of ^{18}O is the ground state of ^{18}Ne (Fig. 1.1). DIAS transitions can

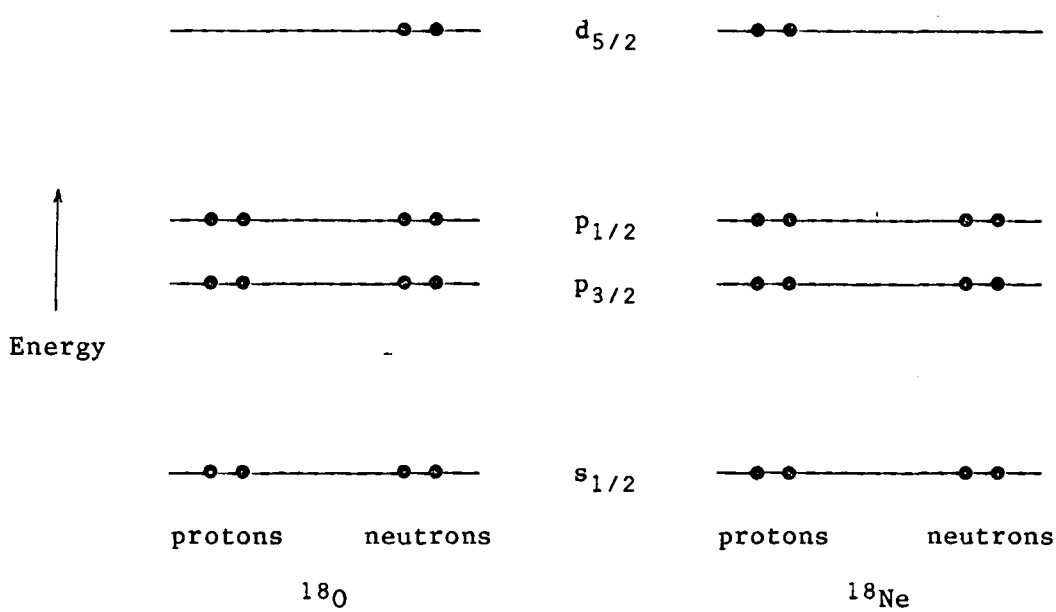

Fig. 1.1 The shell model structure of the double isobaric analogues ^{18}O and ^{18}Ne.

be separated from non-analogue transitions by requiring the emerging pion to have the correct momentum. DIAS transitions are studied because: theoretical calculations are simplfied; there are fewer possible reaction mechanisms; and the cross-sections for DIAS transitions are usually larger

than for any other transitions. In SCX, transitions to the isobaric analogue state (IAS) are studied, e.g. $^{15}N(\pi^+,\pi^\circ)^{15}O(g.s)$.

DCX was first discussed in the 1960's [5]. Physicists saw its potential both to produce proton rich nuclei, and to give nuclear information such as nucleon-nucleon correlations and neutron-proton density differences. There are very few reactions which give this information.

In 1976 Miller and Spencer showed that DCX should indeed be sensitive to correlations and density differences [6]. It is sensitive to correlations because DCX must involve two nucleons - one nucleon cannot remove two units of charge and remain a nucleon. It is sensitive to density differences at energies near the delta (3/2,3/2) resonance: at this energy, the pion interacts so strongly that it does not penetrate the nucleus, and DCX must occur on the surface of the nucleus. If the excess neutron density $\rho_n-\rho_p$ is large at the nucleus' surface then DCX will be enhanced.

DCX differential cross sections are small - typically of the order 1 μb/sr. This meant DCX experiments had to wait until the 'meson factories' TRIUMF, LAMPF and SIN had been commissioned. These laboratories produce high flux beams of pions with a narrow momentum bite. The high flux allows a complete DCX cross-section angular-distribution to be measured in a reasonable time: about 3 weeks in the case of this experiment. The narrow momentum bite allows the DIAS transitions to be resolved from non-analogue ones.

The first successful use of DCX has been in producing proton-rich nuclei [7]. This is useful in testing mass formulae. Other uses have been prevented by gaps in our knowledge of the reaction mechanism; the main aim of DCX cross-section measurements so far, is to understand the reaction mechanism.

1.3 Target Nuclei

One criterion for choosing targets is ease of theoretical calculations. Nuclei with a full core plus either two valence neutrons or two holes satisfy this. In most models the core nucleons are Pauli blocked from taking part, so DCX can involve only the valence neutrons, simplifying calculations. Many nuclei have been studied for DCX, including the two hole nucleus ^{14}C [8], and ^{18}O and ^{26}Mg [9] which have 2 valence neutrons.

1.4 Energy

The energy at which DCX is studied ranges from pion kinetic energies of a few tens of MeV to a few hundreds of MeV. Many measurements have been made at 165 MeV where DCX is dominated by the (3/2,3/2) resonance. However, 50 MeV may prove to be the most interesting energy. Here, cancellation of the 0° form factors for the reaction $p(\pi^-,\pi^0)n$ (f_s = -0.312 + 0.013i, f_p = 0.302 + 0.031i), [10] gives a very small cross-section (Fig. 1.2). This effect remains in heavier nuclei (Fig. 1.2), making the contribution of the 'simple sequential mechanism' small. This mechanism consists of two SCX reactions, with the intermediate state dominated by the IAS (Fig. 5.2). Since the DCX cross section remains large at 0° at 50 MeV for ^{14}C and ^{18}O, other mechanisms must be present; the near absence of the simple sequential mechanism makes these easier to study.

1.5 Models And Previous Experiments

Burman et al. at LAMPF made the first measurement of DCX cross sections [7]. The experiment had low resolution (≃ 4 MeV) so did not disinguish the DIAS transition, and measurements were only made at 0° and 164 MeV. Nonetheless, they showed that the cross section is both small and - by using several target nuclei - sensitive to nuclear structure.

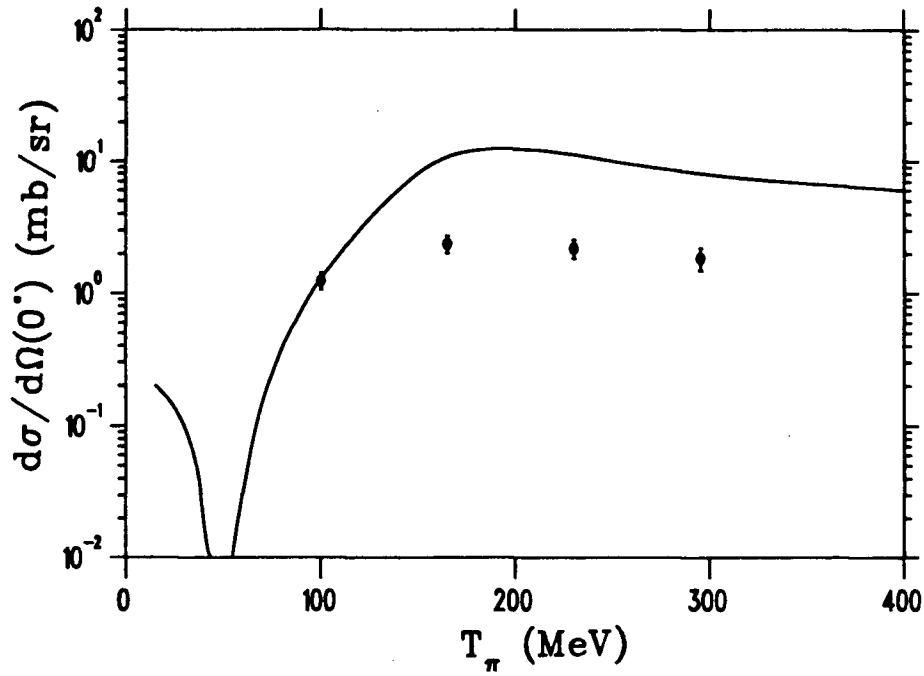

Fig. 1.2 Excitation functions for SCX. (i) curve for $p(\pi^-,\pi^\circ)n$ (ii) data points for $^{14}C(\pi^+,\pi^\circ)^{14}N$ (g.s.) [5]

Seth et al. at LAMPF measured the first angular distribution of DCX cross sections [11]. They used ^{18}O at 164 MeV, over the angular range 13° to 45°. The most striking result was that non-analogue transitions to the 1.89 MeV 2^+ state were as common as analogue transitions. In earlier predictions, based on the simple sequential model, the DIAS transition was always found to dominate; this is because of the large overlap in nuclear wavefunctions for target, IAS and DIAS. This suggested the presence of other important mechanisms.

Since Seth's ^{18}O measurements, several other targets have been used in the energy range 80-300 MeV [12]. The results show that DCX cross sections decrease with increasing A; roughly $\sigma \propto A^{-10/3}$ for T = 1 nuclei (Fig. 1.3). The 164 MeV angular distributions are diffractive with the first minimum

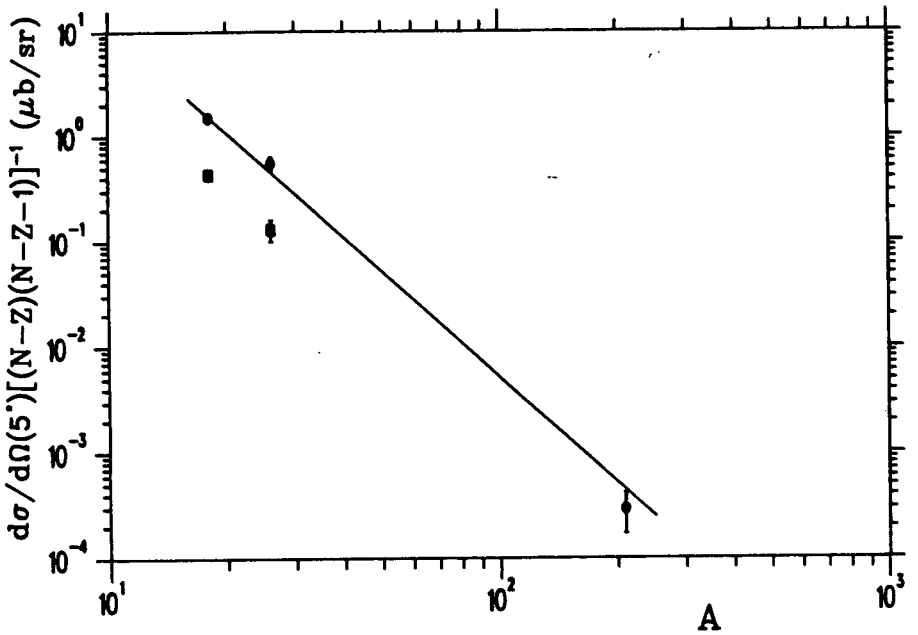

Fig. 1.3 Dependence of DCX on A. Line is $\sigma = 2 \times 10^4\ A^{-10/3}$. Circles are normalized differential cross sections for DIAS transitions from ^{18}O, ^{26}Mg and ^{209}Bi at 5° at 292 MeV. Squares are for ^{18}O and ^{26}Mg at 180 MeV.

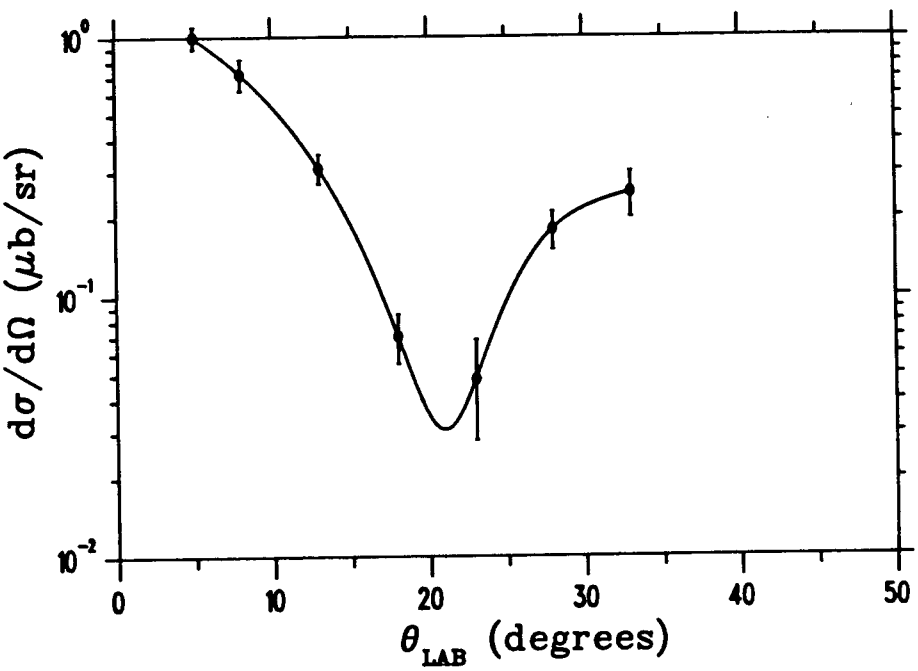

Fig. 1.4 Angular distribution for $^{18}O(\pi^+,\pi^-)^{18}Ne$ (g.s.) at 164 MeV. The shape is diffractive.

between 20° and 30° (e.g. Fig. 1.4). The excitation functions (i.e. variation of cross section with energy) for several nuclei have similar shapes with large variations in this energy range (Fig. 1.5). To be considered successful, a complete theory should reproduce all these features.

The first DCX cross-section angular-distribution at 50 MeV was measured in 1983, when Navon et al. at TRIUMF measured the distribution for ^{14}C [13]. Leitch et al. at LAMPF then repeated this [8] but with better statistical errors and at more forward angles. The main feature of the distribution is the peak at 0°, where the cross section is greater than at 120° by a factor of about 7 (Fig. 4.3).

In 1982, Doron et al. measured the ^{15}N SCX cross section at 165 MeV [14]; They showed that the angular distribution is diffractive. In 1984, Cooper et al. measured it at 48 MeV; they showed that the distribution is forward dipped - the 0° cross section is about one-tenth the 90° cross section (Fig. 1.6). This is similar to the $p(\pi^-,\pi^\circ)n$ reaction.

Navon's results were very different to predictions such as Siciliano's [15]. Siciliano's calculations were based on two sequential SCX; he predicted a 0° cross-section of about 0.2 μb/sr. Navon's data suggested the actual value could be as high as 12 μb/sr, although Leitch later showed it to be nearer 4 μb/sr.

Miller introduced the six-quark bag model to explain the difference [16]. He argued that no conventional mechanism could give DCX forward peaking as high as 12 μb/sr whilst keeping SCX forward dipped and small. He went on to show that Navon's results could be reproduced with the new model. His model introduces quark degrees of freedom into the nuclear wave-function. It postulates that some of the time, the 3-quark bags of the valence neutrons merge together to form a 6-quark bag. The incoming π^+ can give up two units of charge to the 6-quark bag in effectively one stage (Fig. 5.4), greatly

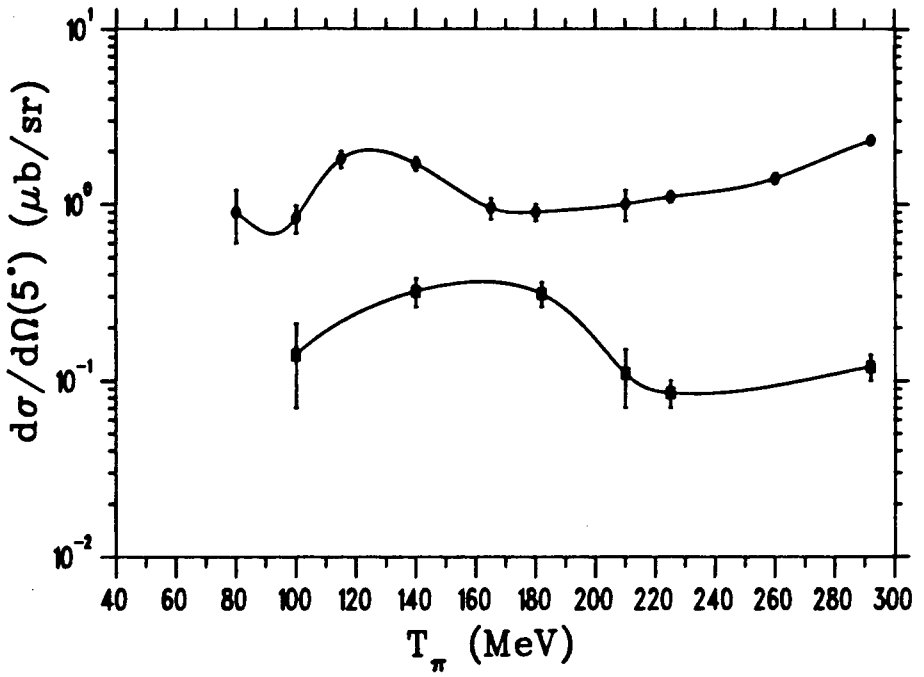

Fig. 1.5 DCX to DIAS excitation functions for ^{18}O (circles) and ^{26}Mg (squares).

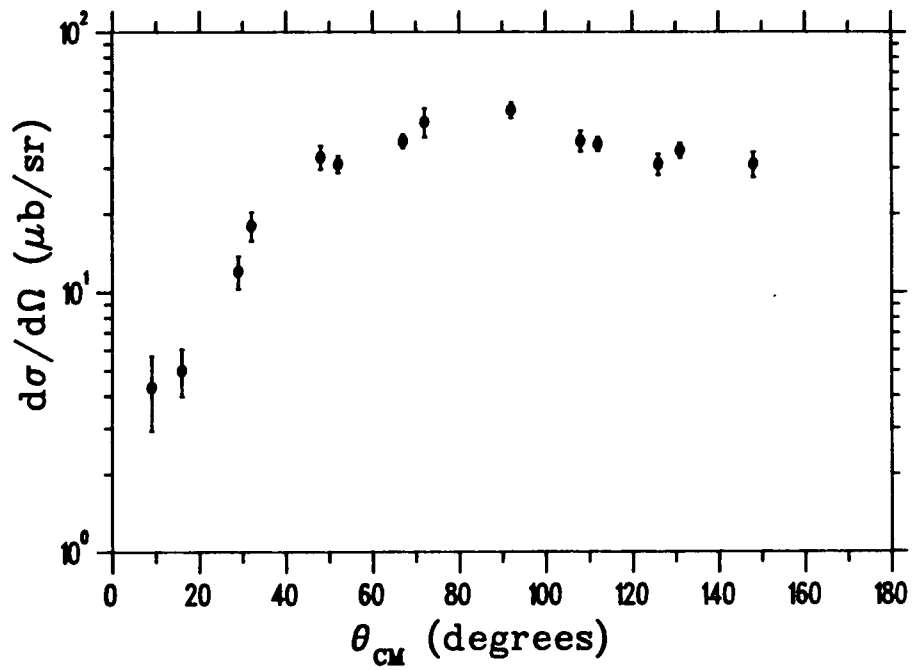

Fig. 1.6 SCX to the IAS angular distribution for ^{15}N, at 48 MeV.

enhancing the DCX cross-section. Six-quark bags have been used to explain other effects, including the EMC effect [17] and the apparent difference of the magnetic moments of free nucleons to those of nucleons in nuclei [18].

Leitch's measurements of ^{14}C DCX at 50 MeV showed a 0° cross section of 4 μb/sr; this means conventional mechanisms may explain the data. When Miller allowed for pion absorption into other channels, he reproduced Leitch's 0° cross section. At the same time Karapiperis & Kobayashi reproduced Leitch's results using a more conventional model, the Δ-hole model [19,20,21]. Pauli blocking prevents DCX from occurring on core nucleons. In the Δ-hole model, core nucleons are excited to a Δ particle, leaving a 'hole state' in the core; the Δ-particle is not Pauli blocked, so this mechanism enhances DCX (Fig. 5.8).

Another model being developed by Jennings and de Takacsy shows that correlations of the valence neutrons also produce forward peaking [22] for ^{18}O DCX with little effect on SCX. These calculations are in an early stage.

The various models differ in their sensitivities to the nuclear core contents. The Δ-hole mechanism involves all nucleons whilst the six-quark bag mechanism and Jennings model involve only the two valence nucleons. So the Δ-hole model is much more sensitive to core contents than the other two. These models are discussed in Section 5.

1.6 Aim Of This Experiment

The aim of this experiment was to give more information on the DCX mechanisms. At 50 MeV the contribution of the simple sequential mechanism to forward angle DCX was small, so that other mechanisms stand out. Previously, 50 MeV DCX angular-distribution data only existed for ^{14}C. Adding to this the distribution for ^{18}O provides information on the A-dependance of DCX.

The results show that the ^{18}O distribution is very similar to that of

^{14}C, in both size and shape. This is as predicted by the six-quark bag model. Initial calculations with the Δ-hole model gave different predictions for the two nuclei; however more recent calculations by Karapiperis & Kobayashi do reproduce the ^{18}O results reasonably well [19]. This possibly arises because the Δ-hole model involves a large contribution to DCX from the 2^+ excited state. Both ^{14}C and ^{18}O have a low-lying 2^+ state.

Clearly further data will be useful in deciding the importance of the various mechanisms for DCX. The 50 MeV DCX cross-section angular-distribution for ^{26}Mg has recently been measured (April 1985) at TRIUMF [23]. Also proposed are measurements of the excitation function for ^{18}O and measurements on ^{34}S and ^{56}Fe [24]. These measurements will lead to a better understanding of the mechanisms for DCX.

2 THE EXPERIMENT

2.1 Beamline

The experiment was carried out on the M13 low-energy pion channel at TRIUMF [25]. The channel was tuned to 50 MeV π^+, with a momentum bite of 0.5%. The primary proton current was typically 130 μA, and the pion-production target used was 2mm graphite: this gave a rate of around 1.1×10^6 π^+/s.

For spectrometer angles less than 30°, the pion beam passes through the first wire chamber. At these angles keeping the wire chamber working properly required a reduction in the rate to 0.35×10^6 π^+/s; this was acheived by reducing the momentum bite.

The beam was monitored mainly by two scintillators (Fig. 2.1), B1 just before the scattering chamber and B2 just after. The number of pions which passed through the target was calculated from the number of coincidences B1.B2.

B2 had to be removed at spectrometer angles 50° or less, because the spectrometer then occupies the usual B2 space. For these angles, two 'muon telescopes' were used to monitor the beam, one fixed above the beam pipe and the other below it. Each telescope consisted of two scintillators at an angle of about 7° to the beam pipe. At this angle the Jacobian for the CM to laboratory frame transformation is nearly constant; this reduces sensitivity to beam direction changes [20]. The telescope counts $\mu_1 \cdot \mu_2$ and $\mu_3 \cdot \mu_4$ were calibrated against B1•B2 at large angles; at small angles the telescope counts were used with the calibrations to estimate what the B1•B2 counts would have been.

As well as pions, the beam contains some muons and electrons. The pion fraction - i.e. the fraction of beam particles that are pions - was

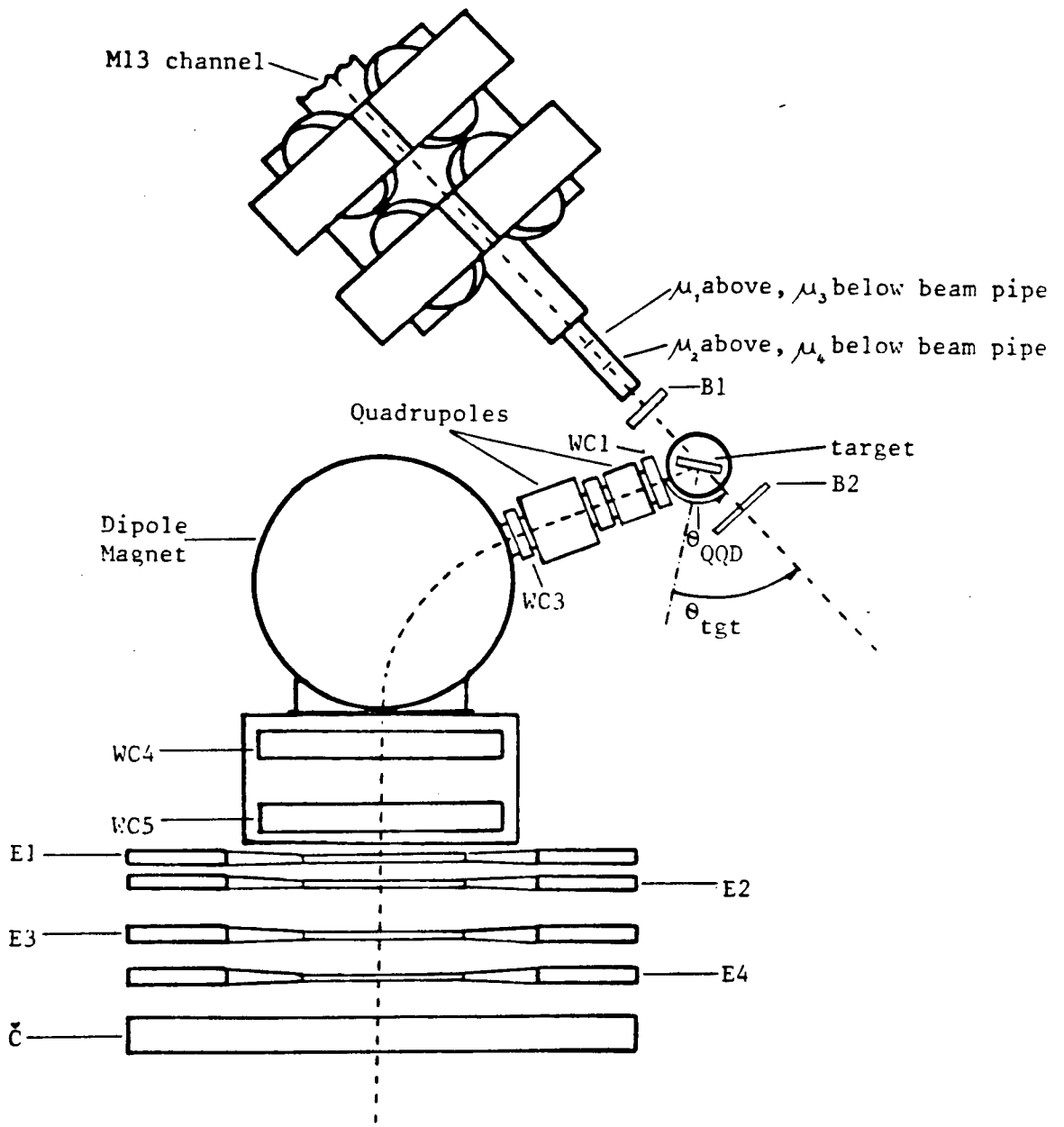

Fig. 2.1 The QQD Low Energy Pion Spectrometer Showing Position Of Target

determined from 'beam sample events' - i.e. coincidences between B1, B2 and a gate generator which was set to ≈ 1s. The beam sample event starts a time-to-digital converter; the stop signal comes when the next pulse of protons passes a capacitive probe in the main beamline. So pions can be distinguished from muons and electrons by time of flight along the M13 channel, called TCAP. Fig. 2.2 shows a typical spectrum.

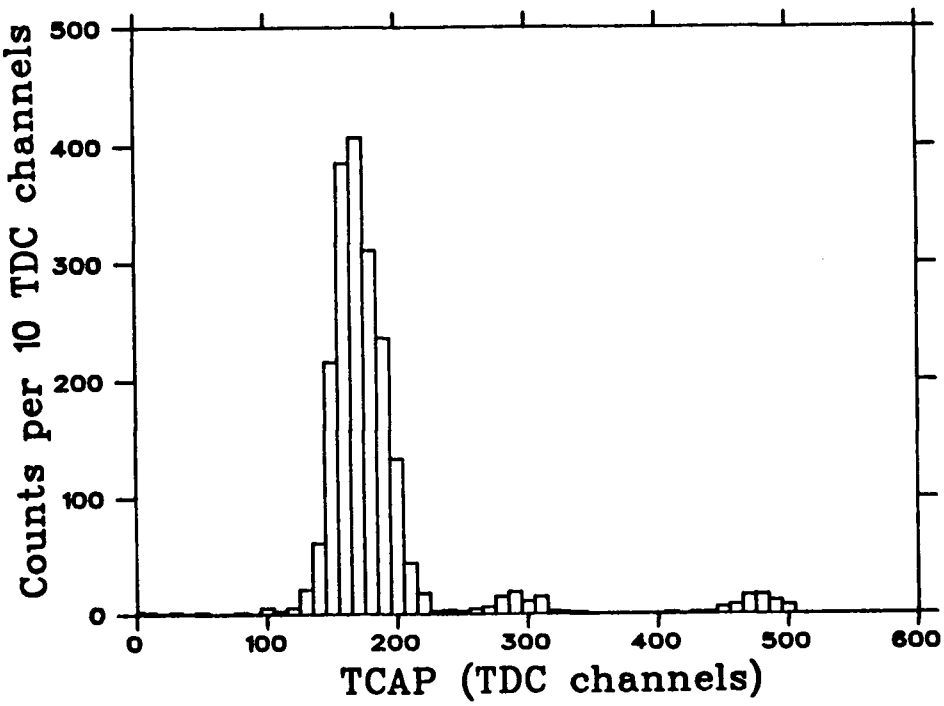

Fig. 2.2 Typical TCAP Spectrum used to estimate the contamination in the incident flux.

2.2 Spectrometer

The QQD low-energy pion spectrometer (Fig. 2.1) [26] was used to measure the momentum of the scattered pions. The spectrometer has two quadrupole magnets and one dipole magnet. The quadrupoles increase the solid angle and the dipole separates pions of different momenta.

This experiment used only the dipole and the second quadrupole QT2, which focusses in the vertical direction. QT1 focusses in the horizontal

direction, increasing the solid angle slightly (~ 5%); but it also reduces resolution in the target traceback (Section 3.4) since it lies between wire chambers 1 and 3 - so it was not used here. There were four scintillators at the exit from the spectrometer, called E1, E2, E3 and E4. In the data acquisition system, a spectometer event was defined as a coincidence B1•E1•E2•E3; such a coincidence was most likely to be caused by a particle passing through the spectrometer. Each time one occured the data acquisition system read details of the event and recorded them on magnetic tape.

The QQD uses four multi-wire proportional chambers - called wire chambers from now on - to measure the tracks of pions. These position-sensitive detectors are described in detail in [3]. Whenever a spectrometer event occurs, each wire chamber gives the x and y coordinates† of where the pion passed through it; the z coordinate is simply the z-coordinate of the wire chamber.

Wire chambers 1 and 3 are at the front-end of the spectrometer. The coordinates from these were used in the target traceback - i.e., the determination of where on the target the pion originated. This allows pions originating from other than the target to be cut - i.e. rejected from analysis.

Wire chamber 1, 3 and 5 coordinates were used to determine the momentum of the pion. A check was made using wire chamber 1, 3 and 4 coordinates: if the two resulting momenta were very different, the event was cut. This is one of the main ways of cutting events in which a pion decayed in the spectrometer. Details of cuts made are given in Section 3.4.

The spectrometer resolution was ~ 1 MeV, resulting mainly from

†We use the standard right-handed orthogonal triple coordinate system for beams: the z-direction is along the beam; the y-direction is vertically up; and the x-direction is to the left of an upright observer facing along the beam.

straggling in the target, wire chambers and the helium gas that filled the target chamber and spectrometer. This easily separated the DIAS transitions from the DCX transitions to the 1.89 MeV first excited state. The solid angle subtended by the spectrometer at the target was 16 msr (Section 3.9).

2.3 Targets

This experiment used ^{16}O and ^{18}O targets in the form of gelled water. The ^{16}O target was included for background measurements but was not needed because the background was very low. The ^{18}O was used for DCX wire-chamber efficiencies and elastic normalizations.

Table 2.1 gives the target compositions. The water was gelled to prevent it bowing the windows of the target holder: at room temperature, the gelled water was self-supporting.

The holder was machined from perspex, to the dimensions shown in Fig. 2.3. 50 μm kapton windows were then glued under tension to the perspex with epoxy resin.

The target water was heated to nearly boiling, and the agar agar gelling agent dissolved in it. The solution was allowed to cool sufficiently to not damage the windows, but not enough to start gelling. It was then syringed into the holder via the filling hole. The filling hole was blocked with epoxy resin. 12 μm aluminium foil was then glued to the kapton, to prevent evaporative loss of water. No glue was used over the target area.

The target mass thicknesses were calculated by dividing the mass of water contained, by the target area. The target area was calculated from the design dimensions.

The targets were mounted on the remote controlled target ladder described in [27]. The target ladder was held in the helium-filled scattering chamber. The target angle - i.e. the angle between the

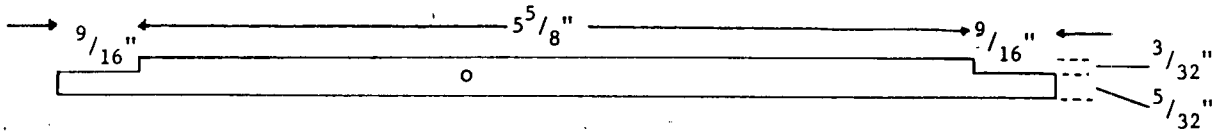

(a)

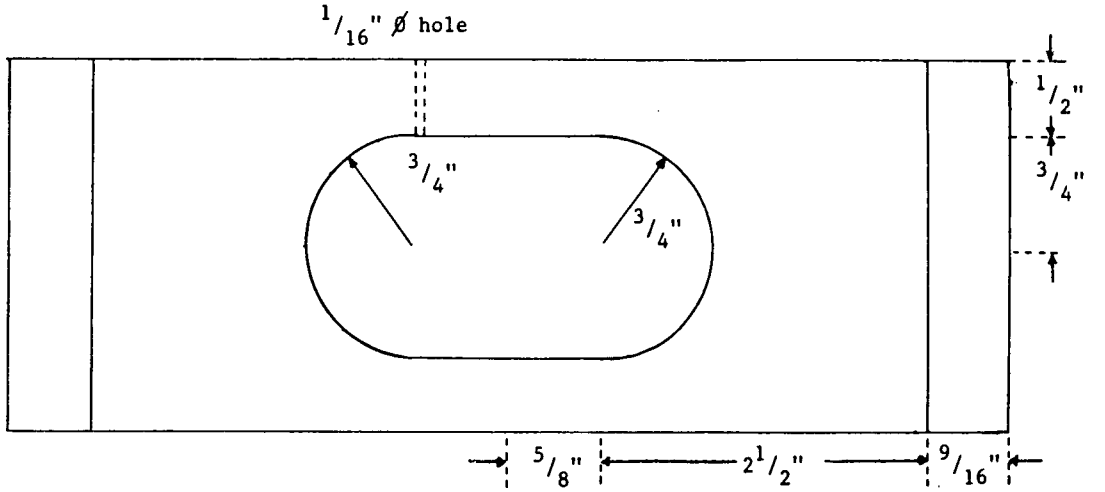

(b)

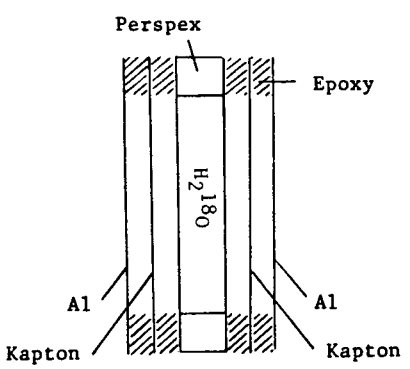

(c)

Fig. 2.3 Target Details

(a) Target holder plan view.

(b) Target holder front elevation.

(c) Schematic target and holder cross section.

Table 2.1 Target Details.

	^{18}O Target	^{16}O Target
Target area (cm^2):	23.50	23.50
Composition (%):		
$H_2{}^{18}O$	94.0	0.2
$H_2{}^{17}O$	2.54	-
$H_2{}^{16}O$	2.50	98.8
Agar Agar	1.0	1.0
Thicknesses		
Gelled Water (g/cm^2)	0.694	0.611
Kapton Window (μm)	50	50
Aluminium Window (μm)	12.5	12.5
Total Window (g/cm^2)	0.017	0.017

target-normal and the beamline - was set to half the spectrometer angle. This minimizes energy straggling because all scattered pions travel the same distance in the target, irrespective of where they scattered. However, at spectrometer angles 40° and 50°, the target angle was 35° and 45° respectively. This was to increase the thickness to give shorter run-times.

2.4 Runs

DCX runs were made at nominal spectrometer angles of 20°,30°,40°,50°,90° and 120° on the ^{18}O target. The dipole was set so that particles of momentum 121 MeV/c passed along the central axis; this corresponds to 45 MeV pions, the energy of the final state pion after a DIAS transition. The angle was changed when the DIAS peak from on-line analysis contained about 80 events, after background subtraction by eye. Each angle took about 3 days.

Elastic runs were made roughly every 12 hours during each DCX run. Both the ^{16}O and ^{18}O targets were used. The polarities of the spectrometer magnets were changed; and the dipole and QT2 were set to a central momentum of 128 MeV/c corresponding to 50 MeV pions. This change of the central momentum between elastic and DCX runs kept the solid angle the same. The purpose of these runs was to measure wire chamber efficiencies and for DCX cross-section normalization.

Some elastic runs were also made at the start of the experiment, using CH_2, ^{16}O and ^{18}O targets. The results of these were used to obtain wire chamber calibrations and magnet transfer coefficients.

2.5 Data Aquisition

The data acquisition system was similar to that used in [3]. A PDP 11/34 computer read data for each event and recorded it on magnetic tape using the standard TRIUMF data acquisition program DA. This responds to a

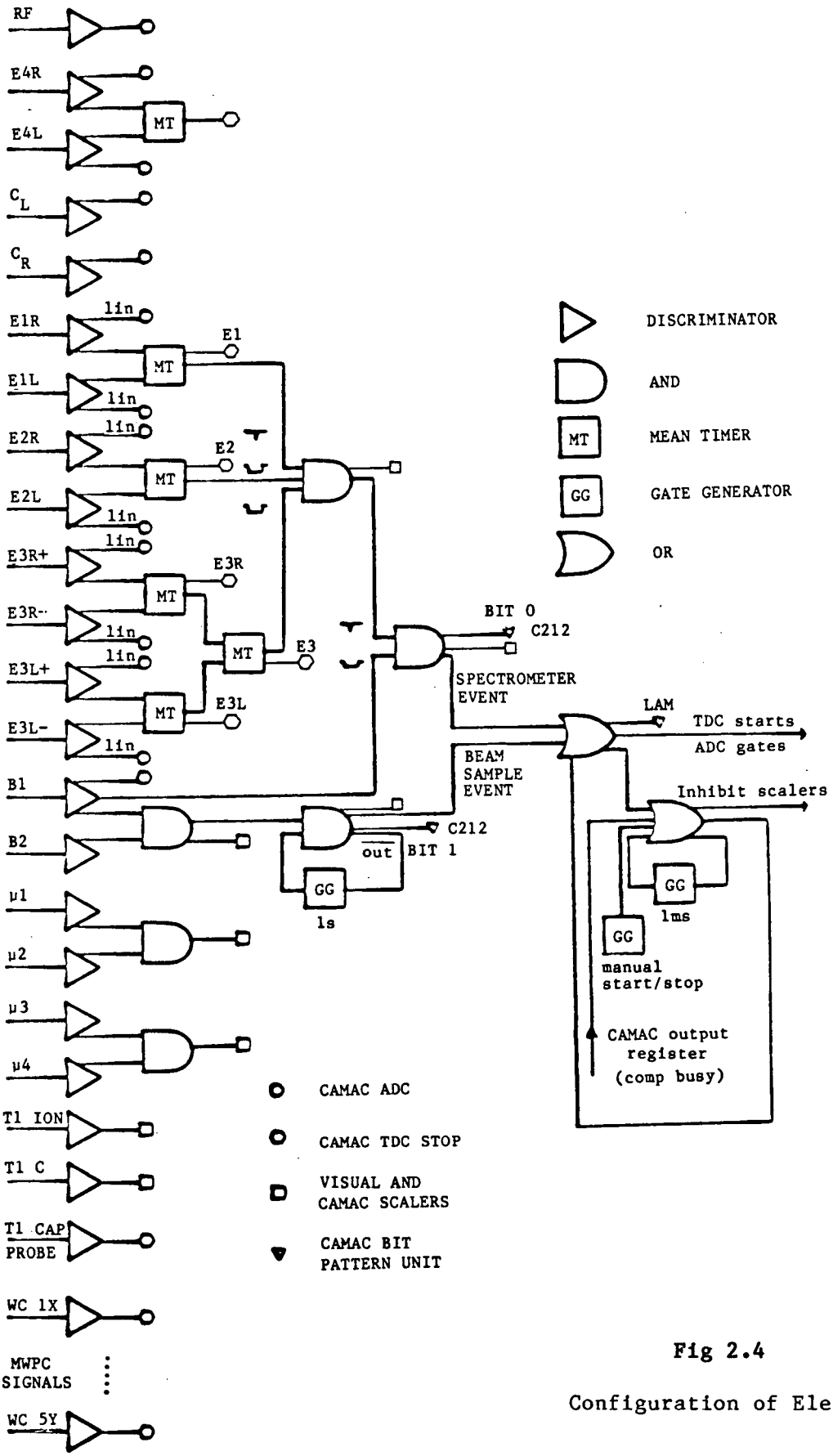

Fig 2.4

Configuration of Electronics

'look-at-me' (LAM) signal by reading information stored in various modules in a CAMAC crate. The LAM was generated for each spectrometer event or beam sample event by a C212 bit-pattern unit in the CAMAC crate. A modified version of the Fermilab program MULTI was used for on-line analysis.

Fig. 2.4 shows the electronics configuration. It includes the following additions which were made to the system used in [3]. The extra muon telescope, $\mu_3 \cdot \mu_4$ was connected to visual and CAMAC scalers. The extra back scintillator E4 was connected to both a time-to-digital converter (TDC) and an analogue-to-digital converter (ADC). The left and right signals from the Cerenkov detector were connected to ADC's. The three back scintillators E1, E2 and E3 were connected to TDC's as well as the usual ADC connections. Various extra visual and CAMAC scalers were also used.

2.6 On-line Analysis

The program MULTI was used for on-line analysis. Early on in the experiment, wire chamber calibrations and magnet transfer coefficients were calculated. These enabled the momenta of the pions passing through the spectrometer to be calculated and histogrammed. Various cuts were applied to reduce background. The cuts were similar to those applied in off-line analysis described in Section 3.4. The cut on time-of-flight from B1 to E1 was particularly important in DCX runs: this removed electrons very effectively to give a clear DIAS peak. This made it easier to judge when sufficient DCX data had been taken for each angle.

3 ANALYSIS

The data was stored on magnetic tapes, and analysed using the TRIUMF programs MOLLI [28] and OPDATA [29]. Several extra subprograms were written for MOLLI.

MOLLI reads data from MULTI-written tapes for each event. It sorts these events into various categories according to user-written subprograms, rejecting 'bad' events from the analysis - e.g. spectrometer events in which only three wire chambers fired. It calculates certain parameters for the remaining good events, such as pion momentum; and it histograms parameters as requested by the user. These histograms are used for example to count the number of events in a particular peak. MOLLI also gives scaler values for each run.

The histograms can be stored for later use such as peak-fitting using OPDATA. OPDATA finds least-squares fits of user-supplied functions to the histograms. This was used here to separate background from the elastic-scattering peaks. Peak fitting was not used for the DCX analysis because of the low background and small numbers of events contained in the peaks.

The first analysis was done early on in the experiment to derive wire chamber calibrations and magnet transfer coefficients - allowing accurate on-line analysis. DCX and elastic runs were analysed after the experiment.

3.1 Wire Chamber Calibrations

This section describes the method used to convert wire-chamber TDC outputs into x,y-coordinates. This method has become standard because it is simple and accurate. It does not require any radioactive sources; instead the taped data from any elastic scattering run can be used, provided it has

enough spectrometer events ($\gtrsim$ 50,000) to give clear histograms. Several runs can be analysed and their histograms summed to build up enough events if wanted.

It would be possible to determine pion momenta directly from TDC outputs, by deriving suitable magnet transfer coefficients. However, these coefficients would then be highly dependent on the electronics: e.g. changing a TDC unit would require deriving a new set of coefficients. It is easier to derive new wire chamber calibrations and keep the old transfer coefficients. This gives greater consistency in the magnet transfer coefficients from experiment to experiment.

3.1.1 Signal Production In Wire Chambers

Fig. 3.1 illustrates the construction of the wire chambers. They consist of three parallel planes of parallel wires. The central plane has horizontal wires and is the anode, which is operated at a high potential (4 to 5 kV). The two cathode planes are earthed. The cathode which measures the y-coordinate has its wires parallel to the anode wires, whilst the x-cathode wires are perpendicular. The cathode wires are insulated at one end and connected to a delay line at the other. The delay lines are earthed at both ends via operational amplifiers.

The signal is produced by electron multiplication forming an avalanche. This occurs over a short length (<0.1 mm) of one anode wire, in the region closest to the track of the particle being detected. The potential of this length of anode wire drops; capacitive coupling then induces a potential drop on the nearby wires in both cathodes. The signal in each cathode wire then travels to the delay line, splits, and travels to both operational amplifiers. These produce the 'minus' and 'plus' pulses. The delay between wires (0.55 μs) is much smaller than the signal dispersion (15 μs) produced

by the delay line. So the signals from several wires merge together before reaching the amplifier.

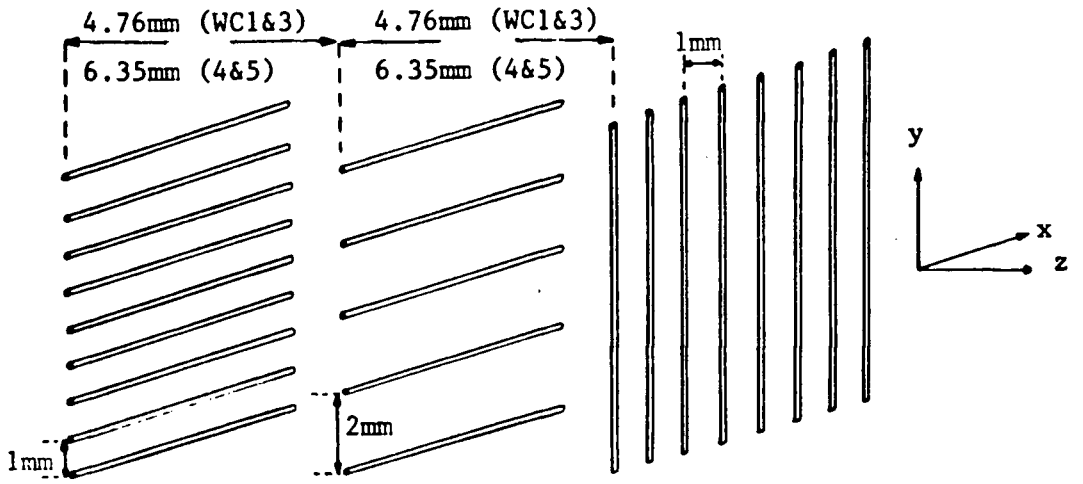

Fig 3.1 Arrangement of wires in QQD wire chambers
(N.B. Table 2.1 in [3] gives the wrong anode and cathode wire spacings).

The x and y signals differ as a result of the different orientations of wires in the two cathodes. Whatever point along the anode the avalanche occurs at, it will be the same distance from y-cathode wires. But this point may be right opposite an x-cathode wire, or anywhere between two of them. So the y-signals are always the same shape, whilst the x-signals can vary. Ideally the peak of the y-signal corresponds to the anode wire on which the avalanche occured; whilst the peak of the x-signal corresponds to how far along the anode the avalanche occurred. For y, this gives a 'picket-fence' structure to a histogram of the time-difference between minus and plus pulses; whilst for x, this histogram is continuous. The picket-fence structure was used to calibrate the wire chambers.

Table 3.1 Wire Chamber Calibrations used and Labelling System.

Label	Wire Chamber Cathode	Slope (mm/TDC channel)	Intercept (mm)
1	WC1X	0.09917	6.00
2	WC1Y	0.09917	5.10
3	WC3X	0.1059	14.30
4	WC3Y	0.1059	-1.50
5	WC4X right	0.09022	-172.80
6	WC4X middle	0.09022	0.50
7	WC4X left	0.09022	203.50
8	WC4Y	0.08889	-3.90
9	WC5X right	0.09144	-197.50
10	WC5X middle	0.09144	0.00
11	WC5X left	0.09144	203.00
12	WC5Y	0.08260	-1.70

3.1.2 Sumcuts

Histograms of the sum of the times of the two pulses are similar for x and y. This sum is a constant amount plus a variable amount. The constant part represents the time taken by a signal to travel the length of the delay line and to the data acquisition electronics. The variable amount is the drift time - the time between the particle passing through the wire chamber and the liberated electrons drifting close enough to the anode to start an avalanche. The drift time varies from zero to 25 ns. Thus ideally sum-histograms would have a square-wave form, with width 25 ns. The observed shape is approximately this but rounded and wider, with a small number of events well outside the 25 ns area. These events are due to misfires of various forms: they can be conveniently removed from analysis by requesting that the sum lies between two values, called sumcuts.

3.1.3 Converting TDC Output To Position Coordinates

The coordinates are derived from a linear function of the difference in TDC outputs for the minus and plus pulses:

$$q_i = m_i \Delta t_i + c_i$$

where i runs from 1 to 12 and labels the cathodes (Table 3.1), Δt is the difference in TDC outputs, q is the position coordinate (x_j or y_j, $j \in \{1,3,4,5\}$ depending on the wire chamber), m and c are the slope and intercept. m and c were determined by analysing an elastic scattering run.

First, values for the sumcuts were determined by analysing the elastic run with the following cuts:

- Only analyse spectrometer events - i.e. test C212 bit pattern

- Ensure all four wire chambers fired: check the minus and plus TDC outputs were within the range given in Table 3.4 for both the x and y cathodes of each wire chamber. (For each of the back chamber x-cathodes, only one of the three sections need fire.)
- If the left x-cathode of a back wire chamber fired, check that the right did not fire too.

The sums of the TDC outputs for each cathode were histogrammed, with 10 TDC channels per histogram bin. The edges of the main body of events for each cathode were then chosen as the sumcuts.

The elastic run was then re-analysed with sumcuts added; this gives clearer picket fences. The following were histogrammed:

- Δt_i for all cathodes, with 10 TDC channels per bin
- Picket fences for all y-cathodes, i.e. Δt_i with 2 TDC channels per bin
- Double hits for back wire chamber x-cathodes: i.e. Δt_i with 10 TDC channels per bin, for each event in which two adjacent x-cathodes fired. These mark the edges of the cathodes.

The slopes and intercepts were determined from these as follows.

(i) Slopes:

All y-cathode slopes were determined from the picket fence histograms. The peaks in each picket fence were numbered in order, and a graph plotted of TDC channel at centre of peak versus peak number. The slope of this graph is the number of TDC channels per 2mm i.e.

$$m_i = \frac{2}{3} \quad \text{mm/TDC channel} \qquad i = 2,4,8,12$$

The x- and y-cathodes in wire chamber 1 were built to the same design with the same methods. The signals were processed by the same TDC unit. So the slope for the x-cathode is taken to be the same as that of the y-cathode; similarly for wire chamber 3, i.e.

$$m_i = m_{i+1} \qquad i = 1,3$$

The slopes for the middle x-cathodes of wire chambers 4 and 5 were determined from the double-hits histograms. The two peaks represent the edges of the cathode. The cathode has 203 wires so is 203 mm long. So if the double peaks are at d_L and d_R TDC channels, then

$$m_i = \frac{203}{d_{Li} - d_{Ri}} \quad \text{mm/TDC channel} \qquad i = 6,10$$

Again the construction of the three sections of each back x-cathode is similar, so the slopes are taken to be the same:

$$m_{i-1} = m_{i+1} = m_i \qquad i = 6,10$$

(ii) Intercepts:

The intercepts for all y-cathodes and the front-chamber x-cathodes were determined from the mean $\overline{\Delta t}_i$ of all events in the Δt_i histogram. The mean was converted to millimetres using the slope:

$$c_i = m_i \overline{\Delta t}_i \qquad i = 1,2,3,4,8,12$$

For the back-chamber x-cathodes, the intercepts were chosen to put the double hits at ± 101.5 mm. If d_L and d_R are the TDC values of the

left-middle and right-middle double hits then

$$c_i = -101.5 - d_{Ri} m_i \quad \text{mm} \qquad i = 5,9$$

$$c_i = \frac{d_{Li} + d_{Ri}}{2} m_i \quad \text{mm} \qquad i = 6,10$$

$$c_i = +101.5 - d_{Li} m_i \quad \text{mm} \qquad i = 7,11$$

Table 3.1 gives the values used for the slopes and intercepts.

3.2 Calculating Pion Momenta

The pion momenta were calculated in a subroutine in the program MOLLI, using the magnet transfer coefficients and some of the wire-chamber coordinates. Rather than working directly in terms of the momentum, the parameter δ is used, defined by:

$$\delta = \frac{p - p_0}{p_0}$$

where p is the pion momentum and p_0 is the central momentum of the spectrometer. The magnet transfer coefficients are explained briefly below; [3] and references therein contain more details.

The pion track through the spectrometer is determined by specifying a set of 5 independent coordinates, e.g. $r \equiv (r_1, r_2, r_3, r_4, r_5) = (x_1, y_1, x_3, y_3, \delta)$. Any other such set, e.g. $r' = (x_5, y_5, \theta_5, \phi_5, \delta)$, can be derived from these. The relation between r and r' is of the form

$$r_i' = M_i + \sum_j M_{ij} r_j + \sum_{jk} M_{ijk} r_i r_k + \sum_{jk\ell} M_{ijk\ell} r_j r_k r_\ell + \ldots \qquad \ldots(3.1)$$

M_i, M_{ij}, M_{ijk} ... are the magnet transfer coefficients.

In particular, x_5 is highly dependent on δ. With $r = (x_1, y_1, x_3, y_3, \delta)$, eqtn. 3.1 for i=5 can be written in the form

$$x_5 = \sum c\, x_1^{\,i}\, y_1^{\,j}\, x_3^{\,k}\, y_3^{\,\ell}\, \delta^m \qquad \ldots(3.2)$$

where Table 3.2 lists the coefficients c used and the values of i to go with each. In this experiment, only linear coefficients of δ were used, i.e. m=0 or 1. So 3.2 can be written as

$$x_5 = A + B\delta$$

$$\Rightarrow \delta = \frac{x_5 - A}{B}$$

where A and B are independent of δ. MOLLI calculated A and B for an event and hence δ.

A second value of δ was calculated using x_4 instead of x_5 with the coefficients given in Table 3.3. This was used as a muon cut (Section 3.4). The two values of δ are denoted δ_4 and δ_5.

3.3 Derivation Of Magnet Transfer Coefficients.

The coefficients c of Tables 3.2 and 3.3 were derived using the method of Tacik and Barnett described in [3] and further developed by M. Rosen [30]. Briefly, the method started with either TRANSPORT [31] coefficients or coefficients from a previous experiment. These coefficients were used to analyse a CH_2-target run made in the current experiment. The δ spectrum has three peaks: ^{12}C ground-state, ^{12}C first-excited state and ^{1}H ground state. The coefficients were then varied to minimize the widths of the three peaks.

Table 3.2 Transfer Coefficients Used to Calculate δ_5.

i	j	k	l	m	c
0	0	0	0	0	-0.86950 E+02
0	0	1	0	0	0.12197 E+01
1	0	0	0	0	-0.83828 E+00
0	0	0	2	0	0.61252 E-02
0	0	2	0	0	-0.12644 E-01
0	1	0	1	0	-0.69003 E-02
1	0	1	0	0	0.80184 E-02
1	1	0	0	0	0.29219 E-02
2	0	0	0	0	-0.18679 E-02
0	0	0	0	1	-0.95040 E+01
0	0	0	1	1	-0.11576 E-02
0	0	1	0	1	0.58393 E-01
0	1	0	0	1	0.21457 E-02
1	0	0	0	1	-0.26014 E-01
0	0	2	0	1	-0.76500 E-04
2	0	0	0	1	-0.14258 E-03

Notation: $x_5 = \sum c\, x_1^{\,i}\, y_1^{\,j}\, x_3^{\,k}\, y_3^{\,\ell}\, \delta_5^{\,m}$ for position coordinates given in mm and δ given in %.

Table 3.3 Transfer Coefficients Used to Calculate δ_4.

i	j	k	l	m	c
0	0	0	0	0	-0.56212 E+02
0	0	0	1	0	0.15673 E-01
0	0	1	0	0	0.16950 E+01
1	0	0	0	0	-0.85318 E+00
0	0	0	2	0	0.47875 E-02
0	0	2	0	0	-0.77813 E-02
0	1	0	1	0	-0.61697 E-02
0	1	1	0	0	0.54586 E-03
1	0	1	0	0	0.45635 E-02
2	0	0	0	0	0.80900 E-03
0	0	0	0	1	-0.65940 E+01
0	0	0	1	1	0.18382 E-02
0	0	1	0	1	0.36602 E-01
1	0	0	0	1	-0.15201 E-01
0	0	0	2	1	0.12953 E-03
0	0	2	0	1	0.68259 E-04
0	1	0	1	1	-0.22782 E-03
1	0	1	0	1	-0.70176 E-04
1	1	0	0	1	-0.14925 E-03
2	0	0	0	1	-0.36080 E-04

Notation: $x_4 = \sum c\, x_1^{\,i}\, y_1^{\,j}\, x_3^{\,k}\, y_3^{\,\ell}\, \delta_4^{\,m}$ for position coordinates given in mm and δ given in %.

3.4 Cuts

Several cuts were used to remove 'bad' events from the δ-histograms. A 'good' event is one where a pion from the target passes through the back scintillators without decaying, firing all four wire chambers. Table 3.4 gives the values of the cuts used. The same cuts were used for both DCX runs and elastic runs, so that the normalization was valid.

(i) Wire Chamber Cut and Efficiences.

Events in which one or more wire chambers misfired (Section 3.1.3) were cut, since all x and y coordinates were needed in the analysis.

Many of the events cut here would have been good events except that a wire chamber misfired. These events are accounted for with 'wire chamber efficiencies', defined as

$$E = \frac{F}{N}$$

where F = number of times the wire chamber fires when N particles pass through it. For elastic runs it is assumed a particle passed through a wire chamber whenever the other three chambers fired i.e. for wire chamber 1

$$N_1 = WC_3 \cdot WC_4 \cdot WC_5$$

so that

$$E_1 = \frac{WC_1 \cdot WC_3 \cdot WC_4 \cdot WC_5}{WC_3 \cdot WC_4 \cdot WC_5}$$

The total efficiency is then

$$E_{tot} = E_1 \cdot E_3 \cdot E_4 \cdot E_5$$

DCX runs have a small rate of good events. This makes chance coincident firings of 3 wire chambers too significant for this method to be reliable. Instead, efficiences from the elastic runs made during each DCX run were used. This is valid because the efficiency only changes slowly with time.

Table 3.4 Values of Cuts used During Analysis.

Wire Chamber Cuts		**Low** (TDC channels)	**High**
(i) Minus and plus pulses	ALL WC's	100	1900
(ii) Sums of pulses	WC1X	1480	1880
	WC1Y	1580	2010
	WC3X	1570	2030
	WC3Y	1710	2180
	WC4XR	1440	1950
	WC4XM	1630	2120
	WC3XL	1450	1950
	WC4Y	1430	1960
	WC5XR	1620	2120
	WC5XM	1560	2050
	WC5XL	1590	2040
	WC5Y	1630	2150
Pion selection	TCAP	80	240
Electron Cuts	E1	480	600

Target traceback	Elastic runs	$\lvert x_0 \rvert < 25\cos(\theta_{QQD} - \theta_{tgt})$ mm
	DCX runs	$\lvert x_0 \rvert < 25$ mm
	All runs	$\lvert y_0 \rvert < 15$ mm
Muon cuts		$\lvert y_4 - y_5 \rvert < 28.0$ mm
		$\lvert \delta_4 - \delta_5 \rvert < 5.0$ %

(ii) Pion Selection (TCAP cut)

The particle-type firing B1 was determined by time-of-flight along the M13 channel. The B1 pulse started a TDC; the stop was the next pulse from a capacitive-probe in the proton beam line. Events in which the TDC value was outside the pion peak (Fig. 2.2) were cut.

(iii) Target Traceback Cuts

Wire chambers 1 and 3 coordinates can be used to determine (x_0, y_0), i.e. where in the target plane the particle originated. This 'target traceback' is found using

$$x_0 = a_1 x_1 + a_3 x_3$$

$$y_0 = b_1 y_1 + b_3 y_3$$

The two coefficients were found from elastic runs using 'picket fence' targets: these have 5 parallel bars $\sim {}^1/_2$cm wide spaced by $\sim {}^1/_2$cm. a_1 and a_3 were determined with a vertical picket fence; they were chosen to make as many events as possible appear to come from the bars and not the gaps. b_1 and b_2 were determined using the horizontal picket-fence target. Table 3.5 gives the values of the coordinates used.

Table 3.5 Target Traceback Coefficients used.

a_1	1.42
a_3	-0.259
b_1	1.28
b_3	0.478

Events which did not originate at the target were cut by limiting x_0 and y_0. This cut is more important for elastic than DCX scattering because the target holder materials have a high DCX Q-value, and so do not contribute to DCX. Consequently the change in target position with target angle was allowed for in elastic analysis but not in DCX analysis.

(iv) Muon Cuts.

About a third of the pions passing through the spectrometer decay via $\pi \rightarrow \mu\nu$; this is allowed for by the decay correction factor (Section 3.8). Many of the muons do not reach the back scintillators, but those that do need to be cut. Two methods were used.

(a) Difference in y_4 and y_5

The quadrupole focusses in the y-direction. It was set to give horizontal pion tracks, which maximizes the spectrometer solid angle. Muons from decays with the μ,ν plane near vertical, have non-horizontal tracks. So tracks with large $|y_5-y_4|$ were cut.

(b) Difference in δ_4 and δ_5

If the μ,ν plane is near horizontal, then x_4 and x_5 differ from their values for no decay. This makes δ_5 differ from δ_4; so events with large $|\delta_5-\delta_4|$ were cut.

(v) Electron Cuts

Cuts (i) to (iv) removed background events well enough to give clean histograms of δ in elastic runs. But the number of π^- events in DCX runs was small, making the remaining e^- events highly significant. In anticipation, a Cerenkov counter was placed after the back scintillators to distinguish electrons from pions. 128 MeV/c electrons have a velocity very close to c and gave a signal; 128 MeV/c pions have a velocity of $\sim {}^2/_3c$ and

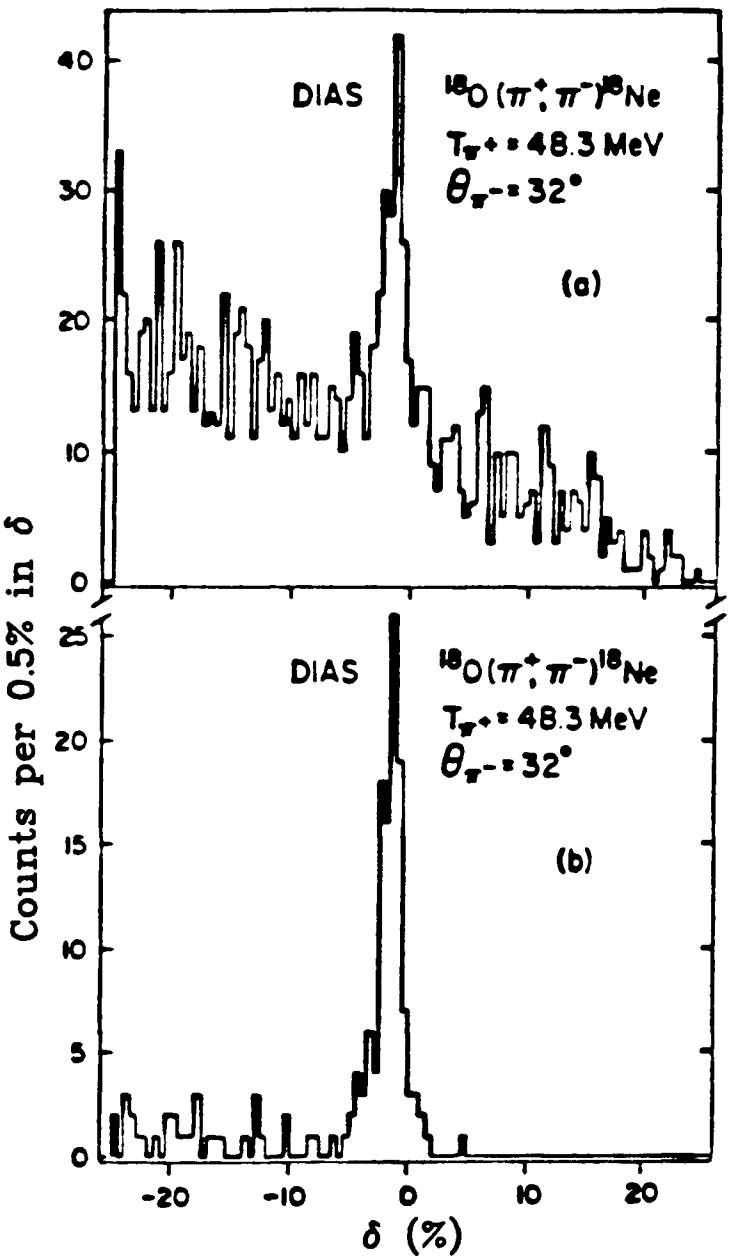

Fig. 3.2 The effects of cuts made during the analysis on DCX δ histograms. In (a) all events which fired all four wire chambers have been histogrammed. In (b) all cuts have been applied.

were not detected. However, the Cerenkov detector was smaller than the back scintillators. This effectively reduces the spectrometer solid angle if used in the analysis.

Instead, a time-of-flight method was used. The journey times for particles to travel through the spectrometer, i.e. from B1 to E1, were measured. 128 MeV/c electrons took ~ 5 ns whilst 128 MeV/c pions took ~ 8 ns: The two can be reliably distinguished with a TDC. This method was checked against the Cerenkov detector, and found to be as effective, with no loss of spectrometer solid angle.

Figs. 3.2(a) and (b) demonstrate the importance of these cuts for a particular DCX run. In (a), only the four wire chamber cut has been used. In (b), all the cuts have been used.

3.5 Peak Size Measurements

Runs for each angle were analysed together using the above cuts. Figs. 3.2(b) and 3.3 show typical δ histograms produced by MOLLI, for DCX and elastic runs. In both cases, the ground state peak is the most prominent feature. To calculate cross sections the number of events in this peak, N_p, must be determined, allowing for background events, N_b.

For DCX runs, the total number of events in the peak, N_t, was counted and found from

$$N_p = N_t - N_b$$

N_b was estimated by fitting a straight line to the data outside, but in the vicinity of, the ground state peak. N_b is then the area under this line and between the limits of the peak. Typically $N_p = 50$, $N_b = 12$.

OPDATA was used to fit the elastic-run ground-state peaks. The fitted function was a Gaussian plus linear background:

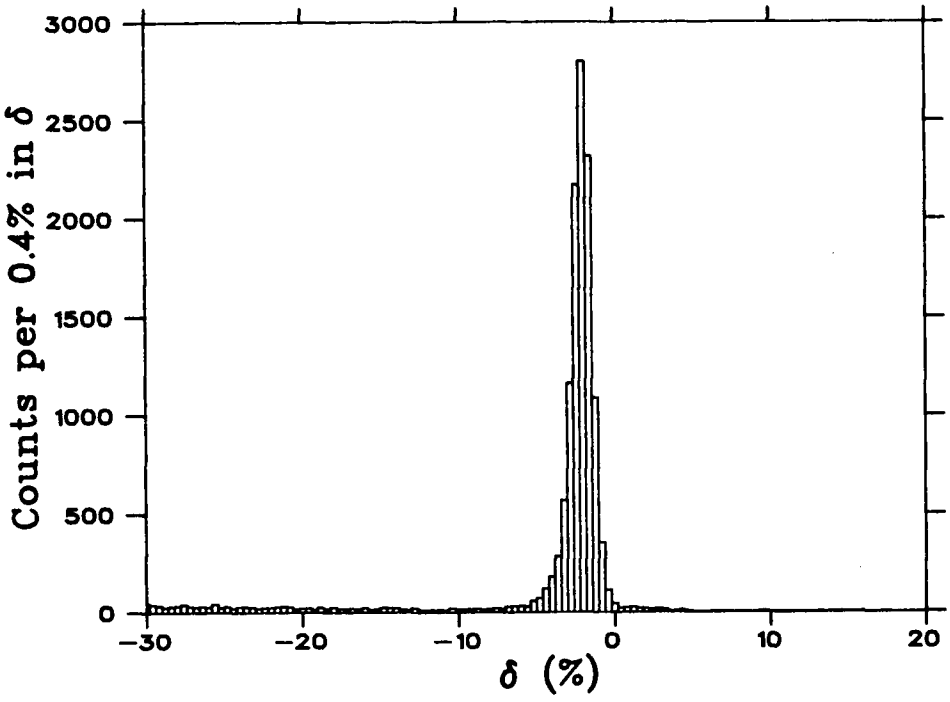

Fig. 3.3 Typical δ histogram for an elastic run.

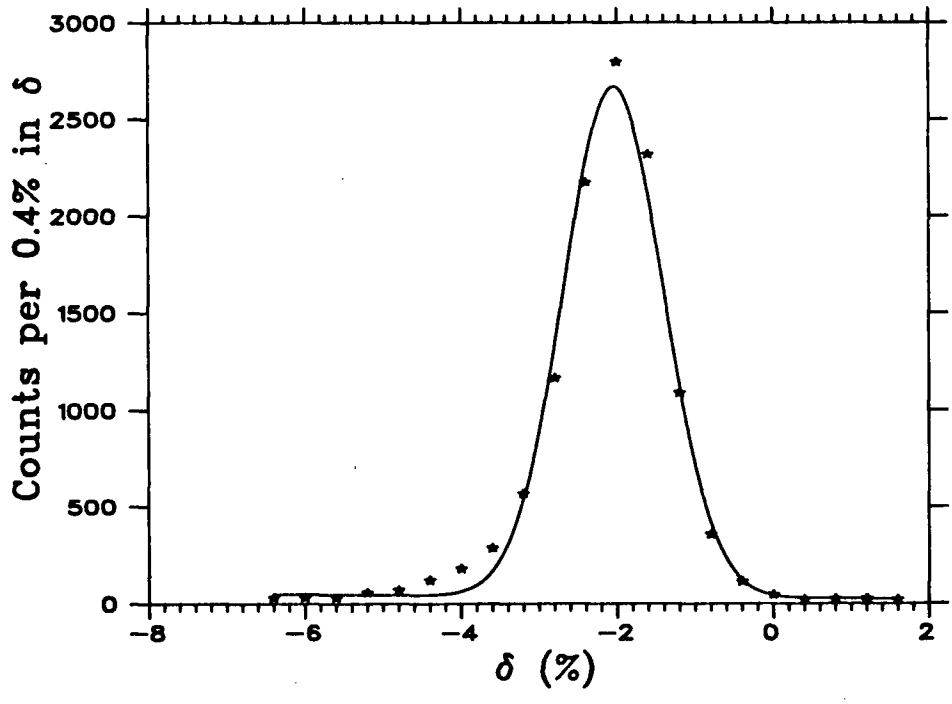

Fig. 3.4 δ histogram for ^{18}O elastic scattering at 30° (data points), with OPDATA fit (solid curve).

$$n(\delta) = m\delta + c + \frac{N_p}{\sigma\sqrt{2\pi}} \exp\left[\frac{1}{2}\left(\frac{\delta-p}{\sigma}\right)^2\right]$$

m and c are the slope and intercept for the background, p is the position of the peak centre, σ is the standard deviation of δ in the peak, and N_p is the best estimate of the number of events without background. Again, N_b was taken to be the area under the linear-background fit between the peak edges. Fig. 3.4 shows a plot of an OPDATA fit. Typically, N_p = 5000, N_b = 600, with χ per degree of freedom = 2. The peaks are Poisson distributions so fitting with a Gaussian underestimates the area by χ^2; N_p was corrected for this.

3.6 Beam Monitoring

A very high proportion of all pions entering the target chamber pass straight through to B2. Thus the scaler monitoring B1•B2 gives the number of pions incident on the target. No dead-time correction was needed: the scalers were stopped whenever the data acquisition system would not detect a spectrometer event - e.g. whilst already processing an event. If two pions pass through B1 and B2 within a short enough time, they give only one pulse. No correction was made for such 'double hits', because the rate is small and fairly constant: it is absorbed in the normalization.

The rate was corrected for contamination using the 'π-fraction', found from the TCAP histogram (Fig. 2.2). The three peaks of this histogram are due to π^+, μ^+ and e^+. The π-fraction is found from

$$\pi_{frac} = \frac{N_\pi}{N_{tot}} \qquad \ldots(3.4)$$

where N_π is the number of events in the π-peak, and N_{tot} is the total number

of events in the histogram. Typically π_{frac}= 97% in this experiment.

B2 could not be used at angles 50° or less; instead the muon telescopes were used. These were calibrated at 90° and 120° against B1•B2, by calculating

$$R_{12} = \frac{1}{2}\left[\frac{B1 \cdot B2(90°)}{\mu_1 \cdot \mu_2(90°)} + \frac{B1 \cdot B2(120°)}{\mu_1 \cdot \mu_2(120°)} \right]$$

with a similar formula for R_{34}. These were used to estmate what $B_1 \cdot B_2$ would have been from

$$B1 \cdot B2(\theta) = \frac{1}{2} \left[R_{12}\mu_1 \cdot \mu_2(\theta) + R_{34}\mu_3 \cdot \mu_4(\theta) \right]$$

At $\theta_{tgt} = 0°$, almost all the beam fell within the target cut boundaries. As θ_{tgt} increases, more and more beam falls outside the x_0 limits. This was allowed for using the 'target efficiency' E_{tgt}, calculated by two methods which gave the same results. Both methods allowed for the changes in beam profile from run to run.

The first method used REVMOC [32]. This simulated the passage of individual pions along the M13 channel, and calculated their coordinates in the target plane. Parameters were adjusted to give the observed beam spot size. E_{tgt} is the ratio of pions falling within the area defined by the target cuts, to the total number of pions reaching the target.

The second method assumed the beam-flux profile was Gaussian in both the x and y directions. The widths were adjusted to the measured beam profile shape. E_{tgt} was taken as the ratio of the integral over the target area to the total integral of the beam flux.

The flux for a run is then

$$\Phi = B1 \cdot B2 \times \pi_{frac} \times E_{tgt} \qquad ...(3.5)$$

3.7 Target Thickness

The target thickness depends on the target angle. If t(0) is the thickness when the target plane is perpendicular to the beam, then the thickness at a target angle θ is

$$t(\theta) = t(0)/\cos\theta \qquad \ldots(3.6a)$$

The target angle was usually chosen to minimize straggle due to electromagnetic scattering: i.e.

$$\theta_{tgt} = \frac{1}{2}\theta_{QQD}$$

- this gives all pions scattered into the spectrometer the same path-length in the target, whatever depth they scattered at. At $\theta_{QQD} = 40°$ and $50°$, larger target angles were used (35° and 45° respectively). This was to decrease running time, by increasing the thickness.

The number of scatterers per unit area of target is then calculated from

$$\mu(\theta) = \frac{t(\theta)N_A}{A} \qquad \ldots(3.6b)$$

where N_A is Avogadro's number and A is the relative molecular mass of the target.

3.8 Π-Decay Correction

About a third of pions scattering into the spectrometer decay before the back scintillators. This is allowed for with a pion-decay correction-factor given by

$$\pi_{dec} = \exp\frac{mL}{\tau c\sqrt{E^2-m^2c^4}}$$

where m, E and τ are the pion mass, energy and mean-life; L is the

spectrometer decay-length.

Pions decaying in the last 5 cm before wire chamber 5 will not be cut in the analysis: the muon position coordinates will be little changed from their undecayed values. So L was taken to be 2.35 m which is 5 cm less than the spectrometer path-length from B1 to wire chamber 5.

3.9 Solid Angle

The spectrometer solid angle used was $\Delta\Omega$ = 16 msr. This was determined from a REVMOC calculation. Pion tracks were randomly generated from the target area at all angles on the spectrometer side of the target. The solid angle was taken as 2π × proportion of tracks which reached E3.

Another method due to Barnett [33] was used to check this value. An elastic scattering run was analysed, calculating the polar angle the pions made with the spectrometer axis. A polar angle ψ was determined for which no pions within the cone defined by ψ collide with the walls etc. of the spectrometer. Then the total number of good events N_t, and the number of events within this cone N_ψ were found for the run. The solid angle was calculated from

$$\Delta\Omega = \frac{N_t}{N_\psi} \times 2\pi(1-\cos\psi)$$

$2\pi(1-\cos\psi)$ is the solid angle of a cone with polar angle ψ. Outer regions of the target lie off the spectrometer axis: this was allowed for in the calculation.

The two methods give the same value, within errors. Also, the solid angle is a constant factor in the cross section calculations; so any error can be absorbed in the normalization.

3.10 Cross Section Calculations

All data needed for the differential cross sections can now be calculated, and used to obtain the cross sections from

$$\frac{d\sigma}{d\Omega} = \frac{N_0}{\Phi\ \mu\ \Delta\Omega} \qquad \ldots(3.7)$$

where $N_0 = \frac{N_p \pi_{dec}}{E_{wc}}$ is the number of pions that scattered into the spectrometer with the required δ.

The ^{18}O elastic cross-sections were compared to those in [3] and [33], to obtain a normalization factor for the DCX cross-sections. The elastic results were very similar (Fig. 4.1) and so the normalization factor was taken to be 1.

3.11 Error Analysis

The cross-sections were calculated from Equation 3.7. Hence the fractional error in the cross section is

$$\left[\frac{\delta(d\sigma/d\Omega)}{d\sigma/d\Omega}\right]^2 = \left(\frac{\delta N_0}{N_0}\right)^2 + \left(\frac{\delta\Phi}{\Phi}\right)^2 + \left(\frac{\delta\mu}{\mu}\right)^2 + \left(\frac{\delta\Delta\Omega}{\Delta\Omega}\right)^2$$

Errors that affect all points equally are absorbed in the normalization. For example the error in solid angle, $\Delta\Omega$, is not included.

(i) Error in N_0

From Equation 3.4,

$$\left[\frac{\delta N_0}{N_0}\right]^2 = \left[\frac{\delta N_p}{N_p}\right]^2 + \left[\frac{\delta E_{wc}}{E_{wc}}\right]^2 + \left[\frac{\delta \pi_{dec}}{\pi_{dec}}\right]^2$$

The error in N_p is the main contribution to error in $d\sigma/d\Omega$. For DCX cross sections, all others are insignificant; for elastic they make a small contribution.

N_p is estimated by making a background subtraction N_b from the total N_t:

$$N_p = N_t - N_b$$

$$\therefore \quad \sigma^2(N_p) = \sigma^2(N_t) + \sigma^2(N_b)$$

and N_t is estimated from

$$N_t = N_p + N_b$$

$$\therefore \quad \sigma^2(N_t) = \sigma^2(N_p) + \sigma^2(N_b)$$

$$\therefore \quad \delta(N_p) \equiv \sigma(N_p) = \sqrt{\sigma^2(N_p) + 2\sigma^2(N_b)}$$

$$= \sqrt{N_p + 2N_b}$$

For elastic runs this error was multiplied by χ per degree of freedom, to allow for the fact that the fit was not ideal.

Error in E_{wc} is mainly due to the random nature of whether a wire chamber fires or not. Assuming a binomial distribution the fractional error was found to be less than 0.005.

Error in π_d was the same for all points, so was not included. It is mainly due to uncertainty in the decay length L: if $\delta L = \pm$ 5cm then

$$\frac{\delta\pi_{dec}}{\pi_{dec}} = \pm\ 0.007.$$

(ii) Error in Φ

From Equation 3.5,

$$\left[\frac{\delta\Phi}{\Phi}\right]^2 = \left[\frac{\delta B1\cdot B2}{B1\cdot B2}\right]^2 + \left[\frac{\delta\pi_{frac}}{\pi_{frac}}\right]^2 + \left[\frac{\delta E_{tgt}}{E_{tgt}}\right]^2$$

For 90° and 120°, $\delta B1\cdot B2$ is negligible. But at smaller angles $B1\cdot B2$ was estimated from the 2 muon telescopes. Using the 2 calibrations - at 90° and 120° - gives 4 estimates for $B1\cdot B2$. The fractional deviation of these from the mean was used to estimate that $\frac{\delta B1\cdot B2}{B1\cdot B2}$ was ±0.01. $\delta\pi_{frac}/\pi_{frac}$ was estimated using binomial statistics; it was typically 0.5 %.

(iii) Error in μ

From Equations 3.6a and b,

$$\left[\frac{\delta\mu(\theta)}{\mu(\theta)}\right]^2 = \left[\frac{\delta\mu(0)}{\mu(0)}\right]^2 + (\tan\theta\ \delta\theta)^2 \qquad (\delta\theta \text{ in radians})$$

Error in $\mu(0)$ was the same for all points and so was omitted. It was largely due to error in target-holder dimensions; the fractional error was estimated to be 0.01.

Error in θ_{tgt} was ± 1° mainly due to uncertainty in alignment of the target-angle scale. Maximum error is at $\theta_{tgt} = 60°$; then $\frac{\delta\mu(\theta)}{\mu(\theta)} = 0.033$

(iv) Error in Spectrometer Angle

A theodolite survey [34] showed the spectrometer-angle scale was 2.0° out. This was corrected for. It is estimated $\delta\theta_{sp} = \pm 0.1°$. This is not shown on the graphs.

(v) Angle-independent Error

The normalization process reduces the angle-independent error. It is estimated to be 12 % from Fig. 4.1.

4 RESULTS

Table 4.1 and Fig. 4.1 show the pion elastic scattering cross sections for ^{18}O. The beam energy is given as 48.3 MeV. This is the average pion energy at the centre of the target, after allowing for the energy loss in the target and windows. Also shown in Fig. 4.1 are the results of other measurements due to Barnett [33] and Tacik [3]. The current results lie between the two sets of data; thus no normalization was applied to either the elastic or DCX data. There is a ± 12% normalization error because of the uncertainty in the previously measured sets of data. The points at 30° and 40° represent new data points for the ^{18}O elastic cross section.

Table 4.2 shows the differential cross sections for pion DCX to the DIAS for ^{18}O. Fig. 4.2 shows that the cross section is a maximum at forward angles and decreases monotonically as the angle increases to 120°. This forward peaking is very different to the SCX cross section for say ^{15}N, which has a minimum at forward angles. The 90° point is the average of runs with the spectrometer both to the left of the beam and to the right.

The data in Table 4.2 is correct. The data published in [35] contains some errors: (i) The cross section at 120° has been revised downwards 7%, as a result of applying target cuts more carefully. (ii) θ_{CM} has been reduced by 4° for the nominal angles 20°,30°,40° and 50° - for these points the spectrometer was to the left of the beam where the 2° scale error should be subtracted [34]; in [35] it was added. The 120° point was measured on the right, so adding the 2° is correct. (iii) The 90° point is the average of runs to the left and right and so has been left at 90° (The decimal arises from transforming to the CM frame).

Fig. 4.3 shows both the ^{18}O and ^{14}C DCX differential cross sections. They have the same size (within 20%) and shape. The similarity suggests that

Table 4.1 Experimental Differential Cross sections for the Reaction $^{18}O(\pi^+,\pi^+)^{18}O$ (g.s.) at 48.3 MeV.

θ_{CM} (degree)	$d\sigma/d\Omega_{CM}$ (mb/sr)
28.3	19.22 ± 0.85
38.4	12.0 ± 0.52
48.5	6.34 ± 0.25
88.6	5.70 ± 0.23
92.7	6.50 ± 0.27
122.6	6.06 ± 0.32

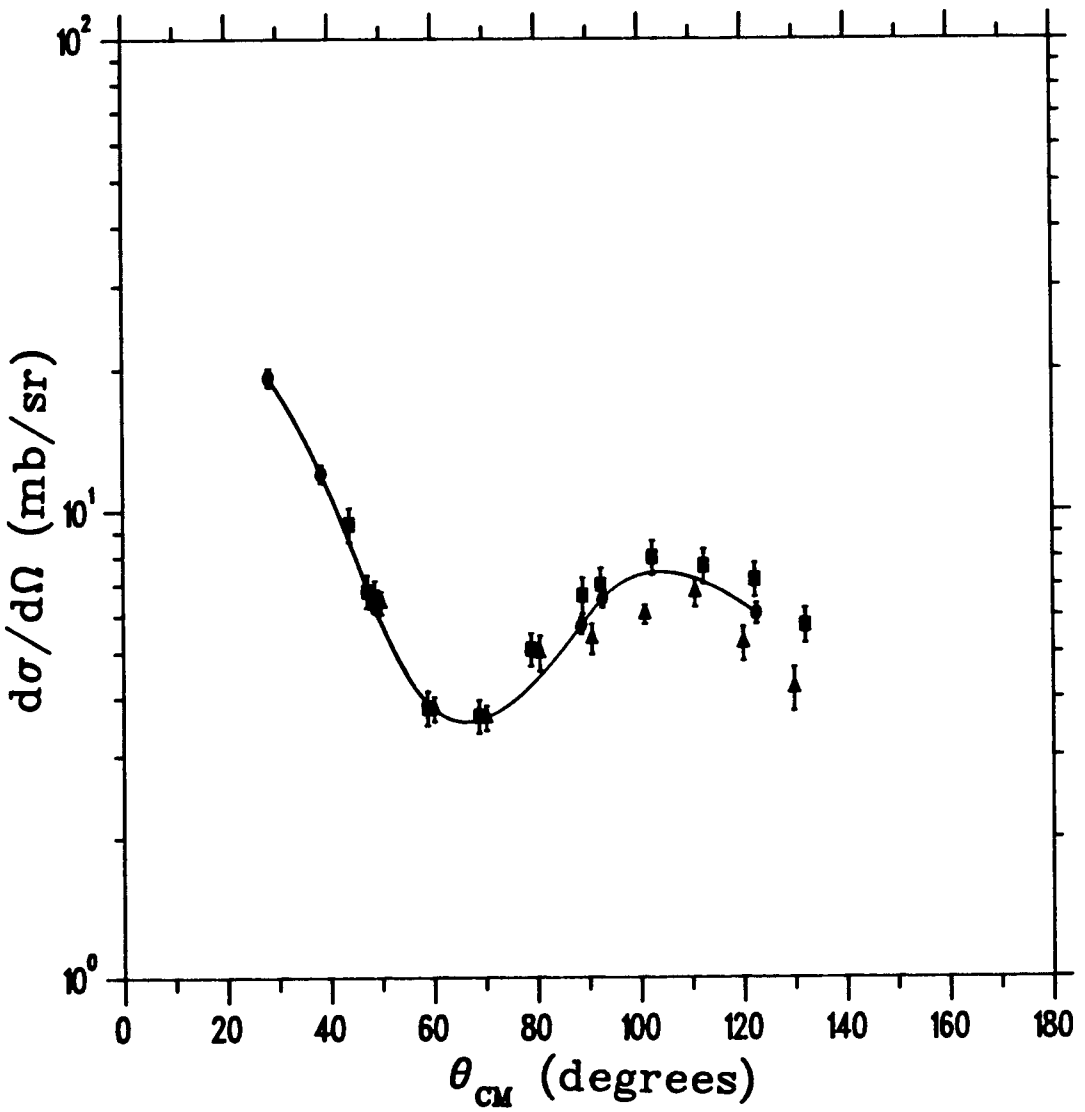

Fig. 4.1 Elastic cross sections used for normalization. Circles - this experiment. Squares - [3]. Triangles - [33]. The curve is to guide the eye.

Table 4.2 Experimental Differential Cross-sections for the Reaction $^{18}O(\pi^+,\pi^-)^{18}Ne$ (DIAS) at 48.3 MeV.

θ_{CM} (degree)	$d\sigma/d\Omega_{CM}$ (μb/sr)
18.2	3.97 ± 1.07
28.3	3.81 ± 0.51
38.4	3.40 ± 0.46
48.5	1.73 ± 0.23
90.6	0.81 ± 0.20
122.6	0.57 ± 0.11

Errors include all angle-dependent sources but not the overall normalization error of 12 %.

Estimated 0° cross-section	4.7 ± 0.5 μb/sr.
Estimated total cross-section	16.2 ± 1.2 μb/sr.

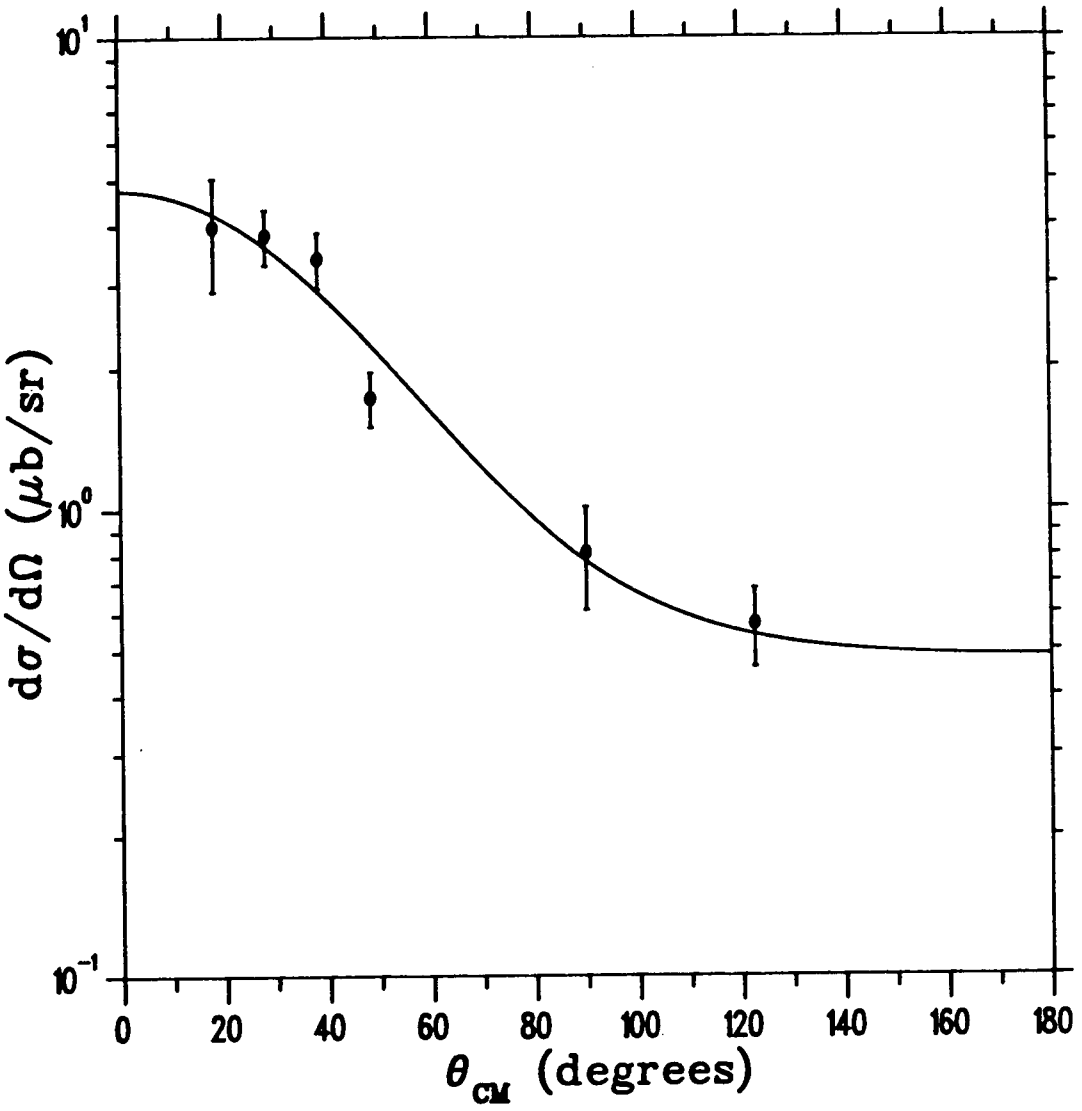

Fig. 4.2 DCX cross sections to the DIAS for ^{18}O. The curve is a fit to the data of the function A $\exp[\lambda(\cos\theta - 1)]$ + B.

either nuclear structure effects are unimportant, or that they are the same for both ^{18}O and ^{14}C. The latter is possible, since in some models the two nuclei are similar: ^{18}O has an ^{16}O core with two extra neutrons, ^{14}C has an ^{16}O core with two holes. However, the 5° excitation functions for ^{18}O and ^{14}C differ in the range 100 MeV to 180 MeV [36], claimed to be an effect of nuclear structure. Another possible explanation is that if the 2^+ excited state gives a large contribution to DCX, then since ^{18}O and ^{14}C both have a low lying 2+ state one would expect similar cross sections.

One theory predicts an $A^{-10/3}$ dependence for DCX cross sections [29]. This is observed at 164 and 292 MeV (Fig. 1.3). Such a dependence would give ^{18}O cross sections less than half ^{14}C cross-sections; this dependence is clearly absent.

The curve in Fig. 4.2 represents a fit to the data of the convenient function $A \exp[\lambda(\cos\theta - 1)] + B$ varying the parameters A,B,λ. This function gives a zero-degree cross section of 4.7 ± 0.5 μb/sr and on integration gives a total cross section of 16.2 ± 1.2 μb.

At backward angles, DCX transitions to the first excited state become important. At 120°, the ground state and first excited state are equally populated (Fig. 4.4). This is similar to Seth's results at 164 MeV [11], although at 50 MeV the excited state is not well populated until larger angles. The ease of transistions to non-DIAS states is evidence of mechanisms other than the simple sequential one via the IAS.

Comparing DCX and SCX excitation functions further contrasts the two reactions. Over the energy range 50 MeV to 164 MeV:

- The 0° DCX cross sections for ^{18}O and ^{14}C <u>fall</u> by a factor 3.5; whilst the 0° SCX cross sections <u>rise</u> by factors 300 for ^{18}O and 340 for ^{14}C. (We have assumed the SCX 0° cross section for ^{18}O is roughly the same as

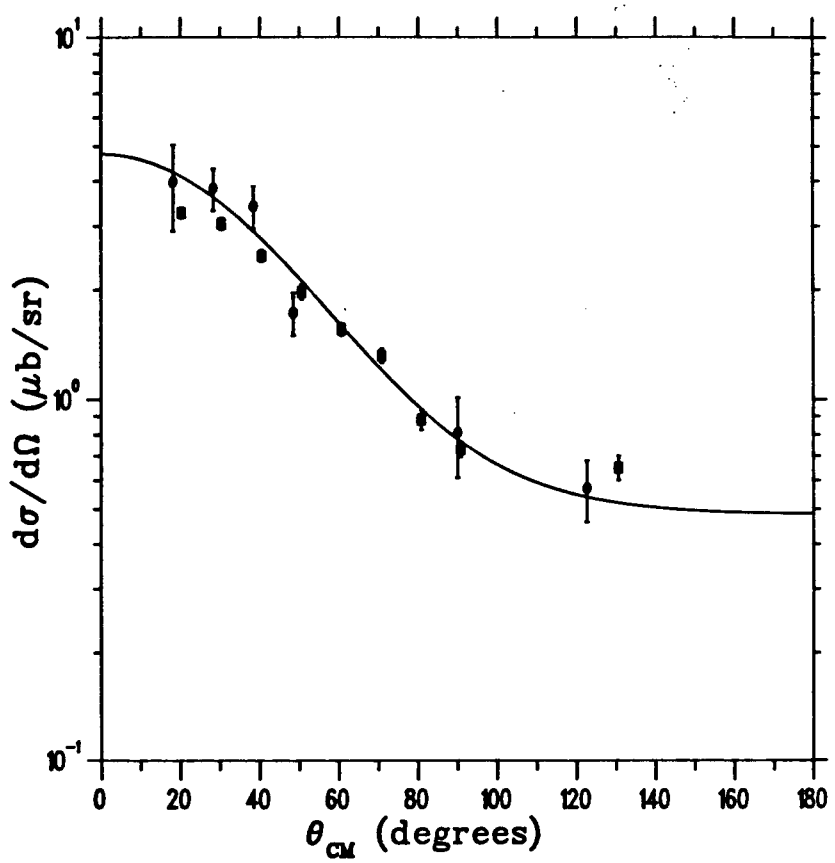

Fig. 4.3 DCX cross sections for ^{18}O (circles) compared to those for ^{14}C (squares) from [8]. The curve is as in Fig 4.2.

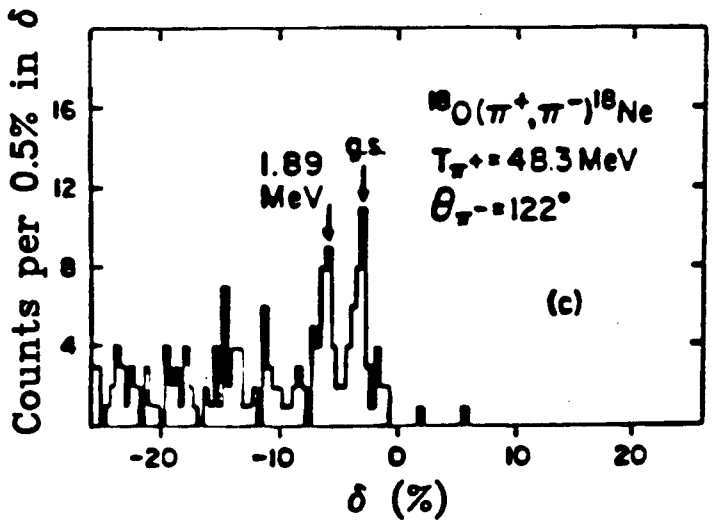

Fig. 4.4 δ Histogram for DCX at 122°.

that of ^{14}C [37]). Also, the 0° cross section for the SCX reaction $\pi^- p \rightarrow \pi^0 n$ rises by a factor of more than 2000.

- The total DCX cross sections for ^{18}O and ^{14}C fall by a factor 10; whilst the total cross section for $\pi^- p \rightarrow \pi^0 n$ rises by a factor 10.

These results provide further evidence that the DCX mechanism is more complicated than the simple sequential one alone. The similarity of the ^{18}O and ^{14}C data is very striking, especially since nuclear structure effects are important in many DCX calculations (e.g. [19]). Further 50 MeV data on other nuclei, e.g. ^{26}Mg will be very useful to determine the importance of nuclear structure effects.

5 THEORY

5.1 INTRODUCTION

Many models exist for calculating charge exchange reactions. This section contains discussion of a selection from these, namely: Coupled-channels optical potential calculations [6,38,39]; the six-quark cluster mechanism proposed by Miller [16 ; recent calculations by Jennings showing the effect of short range correlations [22]; and Δ-hole model calculations by Karapiperis and Kobayashi [19,20,21].

Important calculations not discussed include: Glauber theory calculations, which use the eikonal approximation and are not expected to be valid at 50 MeV; the multiple scattering calculations of Kaufman et al. with the fixed scatterer approximation [40]; and the effects of meson exchange currents (MEC). Oset et al. [41] have calculated meson exchange current effects such as Fig. 5.1 to be small enough to be treated as a correction to other models.

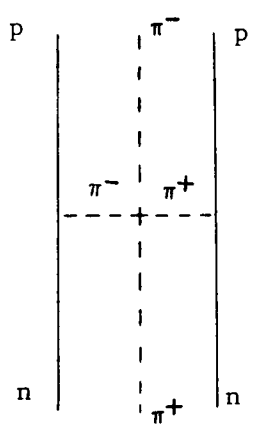

Fig. 5.1 A meson exchange current contribution to DCX.

Understanding the literature requires a reasonable knowledge of scattering theory. The text by Taylor [42] gives a very readable derivation

of the main results for non-relativistic scattering theory. Generalizations to the relativistic case are usually straightforward, such as replacing projectile reduced mass m by CM energy E, and using the Klein-Gordon equation rather than the Schrodinger equation. Some of the central results are listed below.

We consider a scattering system with Hamiltonian $H = H^0 + V$, where H^0 contains the kinetic energy operators and V contains the interaction. Such a system has a transition operator T which obeys a Lipmann-Schwinger equation

$$T(z) = V + VG^0(z)T \qquad ...(5.1)$$

where $G^0(z) = (z - H^0)^{-1}$. The matrix elements of T between initial $|i\rangle$ and final $|f\rangle$ states of the system are related to the amplitude f by

$$f = (2\pi)^2 E\langle f|T|i\rangle \qquad ...(5.2)$$

where E is the total CM energy of the projectile. The cross section for the process $|i\rangle \rightarrow |f\rangle$ is

$$\frac{d\sigma}{d\Omega} = |f|^2 \qquad ...(5.3)$$

The Lipmann-Schwinger equation provides the basis for many approximations, including the Born approximation which includes only the term V on the right hand side of Equation 5.1.

In π-nucleus scattering, the initial and final states often contain different particles. In the scattering discussed here the target nucleus is left in an analogue state , and the π^+ changes charge. The different combinations of particles are known as channels; usually there is an infinite number of distinct channels. This situation can often be dealt with using either the distorted wave Born approximation (DWBA) or optical potential theory, both described in [42].

One of the major goals of π-nucleus theory is to account for π-nucleus reactions in terms of π-nucleon reactions. The usual starting point is the

multiple scattering series, see e.g. Hüfner's article [43] or [1]. This relates the π-nucleus transition operator to a series with terms representing the scattering from 1,2,3...nucleons. Various approximations then allow forms for the optical potential to be derived, with parameters which can be related to π-nucleon reactions. This is the approach of DCX optical potential calculations by Johnson and Siciliano, Miller and Spencer, and others.

5.2 Optical-Potential Model Calculations

The optical potential model is the most frequently used method for describing pion-nucleus scattering. It has successfully been applied to elastic and inelastic scattering [3,4,44] and more recently has been applied to charge exchange reactions [6,39,38]. See [1] for an introduction to the π-nucleus elastic optical potential. Note well that in principle the optical potential accounts exactly for contributions from all excited states [42]; it is in finding approximate forms for the potential, e.g. from multiple scattering theory, that excited-state contributions can be lost.

For charge exchange reactions on T=1 nuclei to the IAS and DIAS, three channels must be kept explicitly; these are

1) π^+ + target nucleus

2) π° + IAS

3) π^- + DIAS

The generalization from one explicit state to three is straightforward; Liu gives the generalization to two channels needed to account for elastic and SCX reactions [45].

The cross sections can then be calculated by solving the resulting coupled-channel Klein-Gordon equations e.g.[6]:

$$(-\nabla^2 + 2EV_\alpha^C - k_\alpha^2)\psi_\alpha = 2E \sum_\beta U_{\alpha\beta}\psi_\beta$$

where V_α^C is the Coulomb potential in channel α, $U_{\alpha\beta}$ is the part of the optical potential causing transitions from state β to α, E and k_α are the pion total energy and its momentum in the final state, and ψ_α is the one-body scattering wave function in channel α. The boundary conditions are [42]

$$\psi_\alpha(\underline{r}) \underset{\underline{r} \to \infty}{\longrightarrow} \delta_{\alpha\beta}\exp(i\underline{k}_\beta \cdot \underline{r}) + f_{\alpha\beta}\frac{\exp(i\underline{k}_\alpha \cdot \underline{r})}{r}$$

hence $f_{\alpha\beta}$, the scattering amplitude from channel β to α, can be determined.

The most general form of an isospin-invariant optical potential is

$$U = U_0 + U_1\underline{\phi}\cdot\underline{T} + U_2(\underline{\phi}\cdot\underline{T})^2$$

where $\underline{\phi}$ and $\underline{T}$ are the pion and nuclear isospin. U_0, U_1, and U_2 are referred to as the isoscalar, isovector and isotensor terms. The U_i, i = 0,1,2, can be related to the π-nucleon phase shifts by making the 'density expansion':

$$U_i = \sum_j U_i^{(j)}$$

where the j^{th} element represents a scattering in which j nucleons act. $U^{(1)}$ is called the first-order optical potential, $U^{(2)}$ the second etc.

Miller in [6] gives an example of simple sequential model calculations along these lines (Fig. 5.2). He considers only isoscalar and isovector terms. First he derives forms for the first order optical potential in terms of the π-nucleon phase shifts. The method uses the multiple scattering series, with the 'coherent' approximation [43]. This restricts the nucleus to the ground state - i.e. the IAS - between scatterings off successive nucleons. At 50 MeV this leads to small, forward dipped DCX predictions in models fitted to SCX measurements [15], because the SCX cross section is

small and forward dipped. This suggests there is a large DCX contribution from non-analogue states. Miller also considers second-order terms, but still omits isotensor terms.

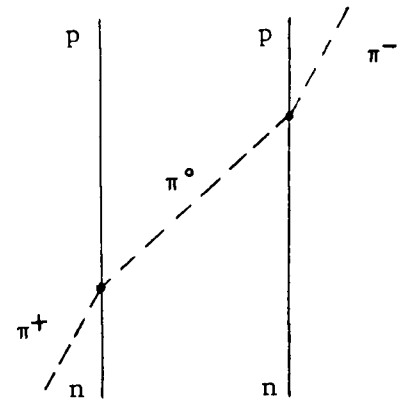

Fig. 5.2 The simple sequential mechanism for DCX.The intermediate state is the IAS. The vertices involve only U_1.

Liu has shown the importance of the second-order optical potential including isotensor terms [39]. He calculates the ^{18}O DCX angular distribution at 164 MeV, and obtains excellent agreement with the data. Previous calculations without isotensor terms wrongly predicted the position of the minimum in the angular distribution. Liu's model fails to predict the 50 MeV data.

Johnson and Siciliano are developing an optical model for charge exchange reactions. They are working towards a comprehensive model which will describe charge exchange at 50 MeV as well as at 164 MeV [46]. However so far most of their work is at 164 MeV. Johnson begins with first-order optical potential calculations in [47]. He relates the A dependence of cross sections to 'geometric' properties of the nucleus: a radius parameter $\bar{R}$, the ratio of valence neutron density to total nucleon density at $\bar{R}$, and difuseness parameters. In particular he explains the

$(N-Z)(N-Z-1)A^{-10/3}$ dependence of DCX cross sections at 164 MeV (Fig 1.3). He predicts DCX to be a sensitive probe of neutron-proton density differences. Whilst the relative A dependence is correctly predicted absolute values are not - presumably due to the omission of second order terms.

In [48] Johnson and Siciliano find a very general form for the second-order optical potential. It contains 4 complex parameters to be fitted to the data. The form is derived by considering various Feynman-like graphs. By using this theoretical motivation they expect the fitted values of the parameters will give information (i) on the structure of the target, and (ii) on two nucleon and other dynamical effects of the pion-nucleus interaction.

DCX is likely to give much information on second-order terms in the optical potential; such information is difficult to obtain by other means. Data at 50 MeV may be especially important since DCX contributions from first-order terms are small. Johnson and Siciliano have not yet published results of any second-order optical potential calculations at 50 MeV. A comprehensive model, capable of predictions at 50 MeV as well as higher energies is needed to realize the full potential of DCX measurements.

5.3 The Six-Quark Cluster Mechanism

The presence of six-quark clusters in nuclei has been suggested as an explanation of the EMC effect [17] and the magnetic moments of the A=3 system [18]. Miller in 1984 suggested they are also responsible for the forward peaking of 50 MeV DCX cross sections [16]. The presence of six-quark clusters in nuclei would introduce quark degrees of freedom into the nuclear wave function in addition to baryons and mesons.

Six-quark clusters can form when two nucleons come close together. Most of the time two nucleons in a nucleus are well separated and behave as

independent particles. But when the distance between their centres drops below some critical distance r_0, they may behave as one particle: this is called a six-quark cluster (Fig. 5.3).

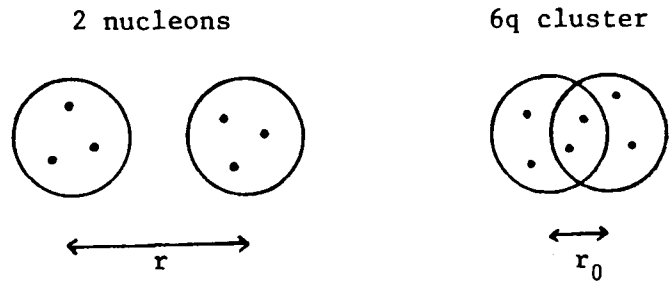

Fig. 5.3 Formation of Six-Quark Clusters

The value of r_0 is constrained. If r_0 is greater than 1.2 fm, nucleon-nucleon scattering data would be hard to explain. If r_0 is less than 0.7 fm, the probability of six-quark cluster formation is too small to give a significant effect. Miller uses $r_0 \simeq 1$ fm: at this distance, the edge of one nucleon is at the centre of the other; 30% of the nucleon volumes overlap.

Miller calculates the probablity of six-quark cluster formation as follows. For DIAS transitions the core nucleons are Pauli blocked, so only the 2 valence neutrons matter. He assumes when the distance between these neutrons is less than r_0 a six-quark cluster forms, with wave function ψ_{6q}; whilst for $r > r_0$ the neutrons have the usual two-neutron wave function $\psi_{nn}(\underline{R},\underline{r})$. $\underline{R}$ is the position for the centre of the two neutron system relative to the nucleus centre; $\underline{r}$ is the vector from $\underline{R}$ to one of the neutrons. Then the probability of finding a six-quark cluster at $\underline{R}$ is

$$P_{6q}(\underline{R}) = \int d^3r \; |\psi_{6q}(\underline{R},\underline{r})|^2 \theta(r_0-r)$$
$$= \int d^3r \; |\psi_{nn}(\underline{R},\underline{r})|^2 \theta(r_0-r)$$

The second equality follows from conservation of probability current. He

uses a product of two p-shell harmonic-oscillator wave functions for ψ_{nn} with b = 1.66 fm for ^{14}C. The total probablity that the two neutrons will be found in a six-quark cluster is then

$$P_{6q} = \int d^3R \; P_{6q}(\underline{R}) = 0.06$$

The simplest six-quark cluster contribution to the DCX amplitude is shown in Fig. 5.4. When the final-state six-quark cluster splits it will form two protons.

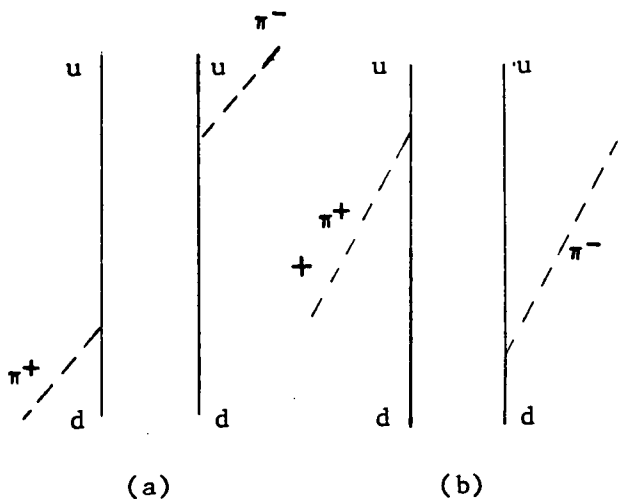

Fig. 5.4 Simplest six-quark cluster contribution to DCX (a) uncrossed (b) crossed terms.

Miller uses products of single-quark wave functions with complete spatial symmetry (6-Symmetry) for the six-quark wave functions. The single-quark wave functions are the lowest energy orbitals of the MIT cluster model.

The two valence neutrons have spin S=0, isospin T=1 and T_3= -1. The initial six-quark state, $|i\rangle$, must have the same. Similarly the final $|f\rangle$ six-quark state must have S=0, T=1, T_3= +1 i.e

$$|i\rangle = |6q,\ S=0,\ T=1,\ T_3= -1\rangle$$

$$|f\rangle = |6q,\ S=0,\ T=1,\ T_3= +1\rangle$$

The pion absorption operator is an axial vector (see Equation 5.). So for pion absorption or emission, $\Delta S = \pm 1$. Then the assumed symmetry of the spatial wave function requires T even. Hence the only possible intermediate states are

$$|m_1\rangle = |6q,\ S=1,\ T=0\rangle$$

$$|m_2\rangle = |6q,\ S=1,\ T=2\rangle$$

Mulders and Thomas [49] have calculated the energies of these states as E_1 = 290 MeV and E_2 = 600 MeV above the mass of two nucleons.

The π-nucleus potential V can be split into two parts, $V = V_1 + V_2$. V_1 is chosen to be the π interaction with the ^{16}O core and the non charge-exchange interaction with the valence neutrons. Then V_2 is the charge-exchange potential operator for the valence nucleons. Its matrix elements are determined by requiring partial conservation of the axial-vector current (PCAC) [1]. They are

$$\langle m|V_2|i\rangle = if\frac{3}{5}u(kR_6)(2E)^{-1/2}\langle m|\sum_{a=1}^{6}\underline{\sigma}_a\cdot\underline{k}\ \tau_a^+|i\rangle \qquad ...(5.4)$$

where E and $\underline{k}$ are the pion total energy and momentum; R_6 is the radius of a six-quark cluster taken to be 1.3 fm [50]; f is the πN coupling constant; $\underline{\sigma}_a$ and τ_a^+ are Pauli spin and isospin operators; and $u(kR_6) \equiv 3j_1(kR_6)/kR_6$ is a form factor to allow for the finite size of the six-quark cluster.

The T matrix elements between target and DIAS states are given by the Born series:

$$\langle f|T|i\rangle = \langle f|V|i\rangle + \langle f|VG^0V|i\rangle + \ldots$$

$$= \langle f|V_2G^0V_2|i\rangle + \ldots$$

where terms with less than two factors V_2 are zero because two charge exchanges are needed. Miller uses the plane wave approximation (PWA), i.e.

he ignores higher order terms. Inserting $1 = \sum_m |m\rangle\langle m|$ gives

$$\langle f|T|i\rangle = \sum_m \langle f|V_2 G^0|m\rangle\langle m|V_2|i\rangle$$

For the uncrossed diagram,

$$G^0|m_j\rangle = \frac{1}{E-E_m}$$

whilst for the crossed diagram

$$G^0|m_j\rangle = \frac{1}{-E-E_m}$$

Adding these and taking into account the probability of finding a six-quark cluster gives

$$\langle f|T|i\rangle = \tilde{P}_{6q}(\underline{q}) \sum_m \frac{2E_m}{E^2-E_m^2} \langle f|V_2|m\rangle\langle m|V_2|i\rangle$$

where $\tilde{P}_{6q}(\underline{q})$ is the Fourier transform of $P_{6q}(\underline{R})$.

So far no allowance has been made for absorption i.e. $\pi NN \rightarrow NN$. When this is allowed for the model gives the curve in Fig. 5.5 for ^{14}C [50]. The model is seen to reproduce forward angle DCX scattering well although the forward peaking is too pronounced. At other angles, more conventional mechanisms can account for DCX since the $p(\pi^+,\pi^\circ)n$ amplitude is larger. The six-quark mechanism involves only the valence neutrons. This makes the predicted distribution for ^{18}O very much the same as for ^{14}C.

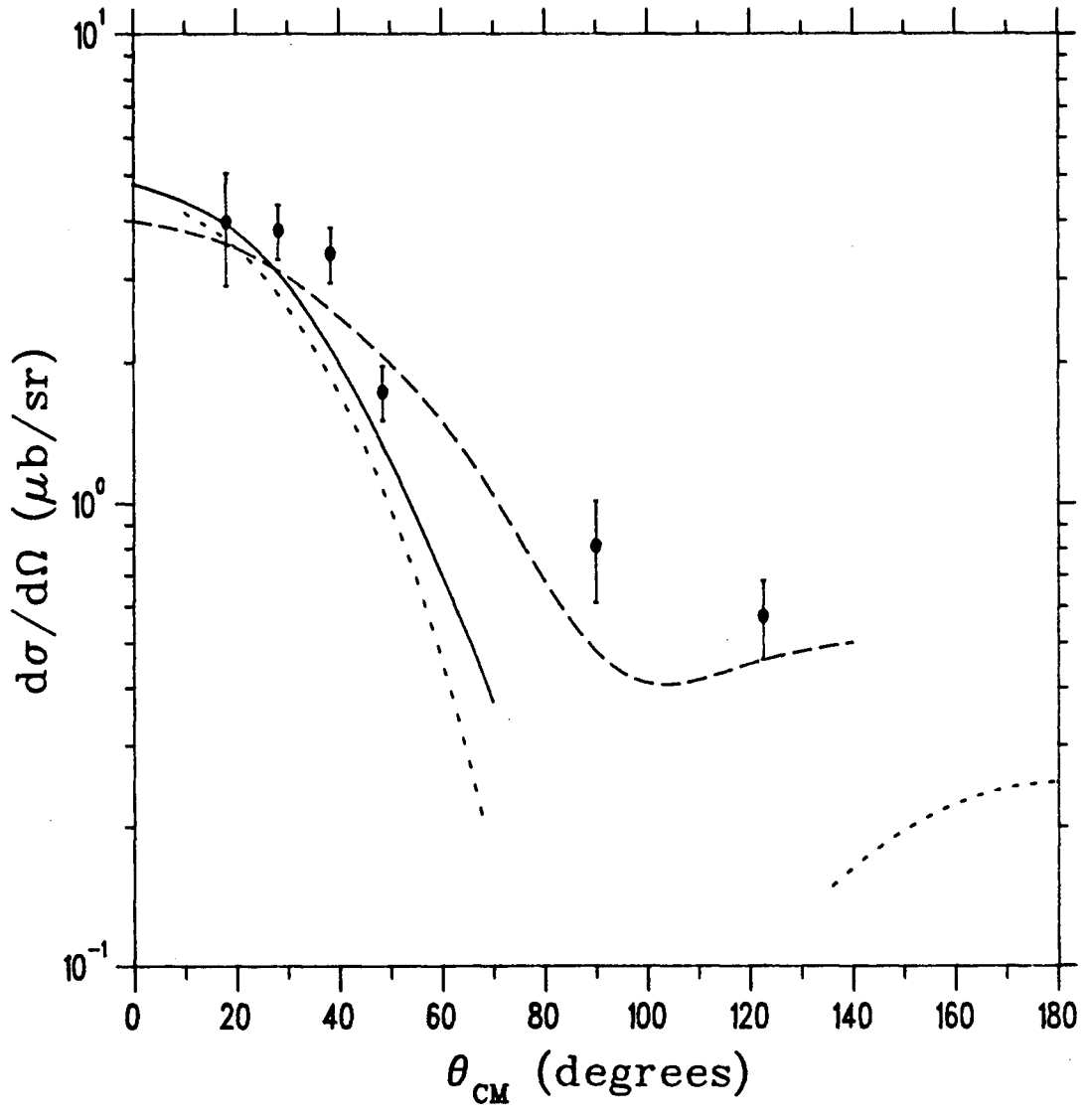

Fig. 5.5 Comparison of theoretical predictions with measured 50 MeV ^{18}O DCX data.
(a) Solid line: Six-quark cluster contribution for ^{14}C.
(b) Dotted line: Jennings and de Takacsy's predictions.
(c) Dashed line: Δ-hole model calculation.

The PWA neglects higher-than-$V_2G^0V_2$ terms in the Born series. Multiple scattering terms such as $V_1G^0V_2G^0V_2$, representing three scatterings may be expected to be large. Such terms could be accounted for by using distorted waves to represent scattering to all orders by V_1. However there is evidence that such corrections are small [51] at 50 MeV.

The six-quark clusters do not contribute to DCX at higher energies. This results from the rapid decay of the intermediate states $|m\rangle$ into two nucleons and a π above E ≈ 100 MeV.

The same input gives a six-quark cluster contribution to SCX which is roughly 0.3 times the contribution to DCX. Miller claims this is a result of interference between terms with different intermediate states. Six-quark clusters involving a core nucleon and a valence neutron can also contribute to SCX; but the Wigner-Eckart theorem implies summing over all such pairs gives zero provided the core has equal numbers of neutrons and protons.

When Miller's paper [16] was published, only the data for 50 MeV ^{14}C DCX of Navon [13] was available. This suggested the 0° cross section was as high as 12 μb/sr. Miller discusses several possible contributions to DCX. He shows none can produce DCX 0° cross sections as high as 12 μb/sr whilst keeping SCX small and forward dipped. Leitch's measurements [8] showed the 0° cross section was only 3.9 ± 0.5 μb/sr, similar to the ^{15}N SCX 50 MeV cross section. In view of this, Miller concluded that other mechanisms could explain DCX, but that the six-quark cluster mechanism could not be ruled out [52].

5.4 Effect of Short Range Correlations

Recent preliminary calculations by Jennings and de Takacsy have reproduced forward peaking. In their model short range correlations between the valence neutrons cause the backward DCX cross section to be small. The

model is at an early stage of development; so far only a simple model has been used which requires rather a high closure energy to fit the data.

The importance in nuclear physics of nucleon-nucleon correlations has been stressed by many authors, including Ericson and Ericson [53], and Eisenberg et al. [54]. Correlations are expected to have large effects on DCX because the reaction must involve at least two nucleons.

Correlations can be viewed as arising from σ and ω meson exchange. This does not contribute to elastic scattering, where the exchanged particle must carry charge. For DCX though, the exchanged particle need only transfer energy and momentum. Fig. 5.6 illustrates the mechanisms dealt with. The exchanged particles are not treated explicitly. Instead their effect is included in the wave function of the two valence neutrons by using a Gaussian dependence on the relative coordinate.

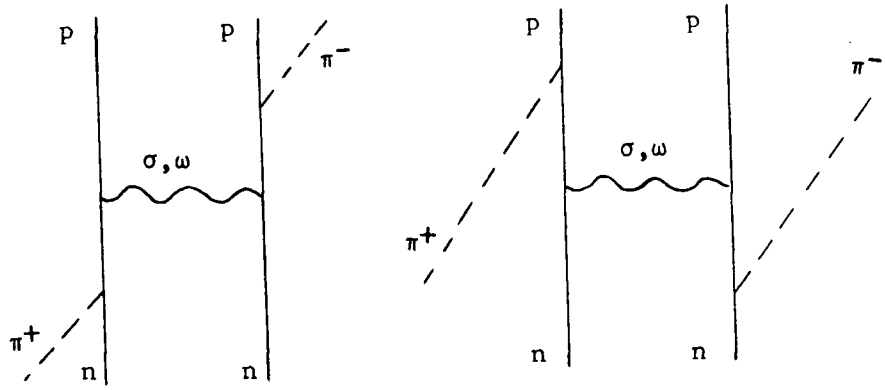

Fig. 5.6 The mechanisms considered by Jennings and de Takacsy.

A similar treatment to Section 5.3 gives

$$T = \sum_m \frac{2E_m}{E^2 - E_m^2} \langle f|V|m\rangle\langle m|V|i\rangle$$

where now the intermediate states are shell-model excitations of ^{18}F. Using the closure approximation

$$\sum \frac{|m\rangle\langle m|}{E-E_m} \approx \frac{1}{E-\bar{E}}, \quad \text{where } \bar{E} \text{ is the closure energy, gives}$$

$$T = \frac{2\bar{E}}{E^2-\bar{E}} \langle f|VV|i\rangle$$

The potential operator V producing charge exchange is analogous to Miller's but has operators defined on nucleons rather than quarks, and is summed over the valence neutrons:

$$V = -if(2E)^{-1/2} \sum_{a=1}^{2} \underline{\sigma}_a \cdot \underline{k}\ \tau_a^+$$

The states are taken to be

$$|i\rangle = \psi(r_1,r_2)\ |S=0,\ T=1,\ T_3=-1\rangle$$

$$|f\rangle = \psi(r_1,r_2)\ |S=0,\ T=1,\ T_3=-1\rangle$$

with the spatial wave function

$$\psi(r_1,r_2) = C\,{}_1F_1(-N;{}^3/_2;2bR^2)\ \exp(-bR^2 - \tfrac{a}{4} r^2)$$

where ${}_1F_1$ is a confluent hypergeometric series, C is a normalization constant, $\underline{R} = {}^1/_2(\underline{r}_1+\underline{r}_2)$, $\underline{r} = \underline{r}_1-\underline{r}_2$. For ^{18}O, N is usually taken to be 2 whilst for ^{14}C it is 1. In the shell model the parameter b is usually taken to be 0.33 fm^{-2} for ^{18}O and the correlation parameter a = b.

These wave functions give

$$T = \frac{1}{(2\pi)^3} \frac{2}{E} \frac{2\bar{E}}{E^2-\bar{E}^2} f^2 \, k^2 \cos\theta \, \exp\left(\frac{-K^2}{2a} - z\right) P_N(z)$$

where $k = k_i = k_f$, $z = q^2/8b$, $\underline{q} = \underline{k}_i - \underline{k}_f$, $\underline{K} = {}^1/_2(\underline{k}_i + \underline{k}_f)$ and P_N is a polynomial of degree 2N. For N = 2,

$$P_N(z) = 1 - \frac{8}{3} z + \frac{44}{15} z^2 - \frac{16}{15} z^3 + \frac{2}{15} z^4$$

The factor $\frac{1}{(2\pi)^3}$ depends on the wave function normalization; with this normalization Equations 5.2 and 5.3 give the cross section. The sum over two neutrons gives one of the factors 2 in the numerator.

The closure energy can be treated as a free parameter. A value $E \approx 7$ MeV fits the data best. This is a little high in view of the energy levels of ^{18}F (Fig. 5.7). If the low lying states are the main contributors to DCX one would expect a smaller closure energy. This is an indication the model is an oversimplification.

The above input gives the curve shown in Fig. 5.5. The strong forward peaking arises largely from the cosθ factor in T. The cross section is small at back angles (large q) because of the factor e^{-z}. The forward cross section decreases rapidly with energy because of the factor $\exp(-k^2/2a)$, in agreement with the data.

The contribution of this mechanism to the SCX transition operation is a factor 2 smaller. Assuming no complications from interference, this gives a factor 4 smaller in the cross section. The factor 2 arises from the form of the operator $\underline{\phi}.\underline{\tau}$, see e.g. [55].

Thus this simple model with conventional mechanisms can explain the

data. Exotic mechanisms such as six-quark clusters seem unnecessary.

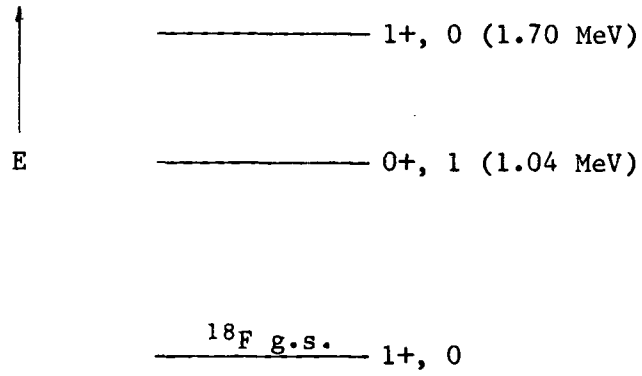

Fig. 5.7 ^{18}F energy level diagram.

5.5 The Δ-hole Model

The Δ-hole model successfully accounts for elastic, inelastic and SCX π-nucleus scattering near resonance energy [56]. Karapiperis and Kobayashi have recently applied the model to DCX reactions [19,20,21]. They reproduce data for ^{14}C, ^{16}O and ^{18}O from 50 MeV to 164 MeV with reasonable success, except for ^{18}O above 100 MeV. For an introduction to the Δ-hole model, see [4] and references therein.

The main improvement of the Δ-hole model over standard optical potential models is in the treatment of the nuclear state between scatterings in multiple scattering theory. At resonance energy, π-nucleus scattering is dominated by the Δ(1232) resonance. In the Δ-hole model this resonance is treated as a Δ-particle coupled to a nucleon hole in the nucleus; the effects of the propagation of this Δ-hole through the nucleus is allowed for explicitly. In standard optical models these effects are omitted by making various approximations, e.g. the 'factorization approximation' [4].

At 50 MeV resonant Δ production is very small. There are some problems

with the Δ-hole model for elastic scattering at this energy [58], and these persist for DCX. But Karapiperis and Kobayashi claim DCX presents no new problems for the Δ-hole model.

The Δ-hole model calculations are detailed and fairly complicated. They are briefly summarized below. The results are also summarized with emphasis on ^{18}O.

The transition operator for DCX is split into two terms, the sequential and the Δ-hole mechanisms (Fig. 5.8)

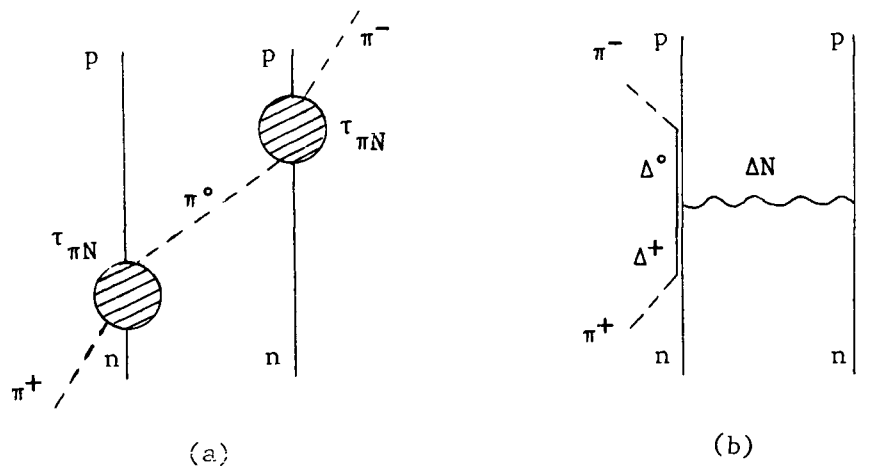

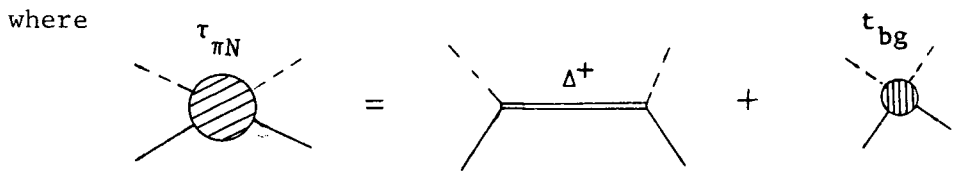

Fig. 5.8 The basic DCX mechanisms in the Δ-hole model. (a) Sequential (b)Δ-hole.

The matrix elements of the sequential DCX transition operator are then

$$\langle f|T_{seq}|i\rangle = \langle f,\text{distorted}|\tau_{\pi N}G^0\tau_{\pi N}|i,\text{distorted}\rangle$$

where

$$\tau_{\pi N} = V^{\dagger}G_{\Delta N}V + t_{bg}$$

The operator V allows for nucleon motion via the form factor $v(\kappa^2)$ and by using the π-nucleon relative momentum $\underline{\kappa}$:

$$V = f\ v(\kappa^2)\ \underline{\kappa}.\underline{\sigma}\ \tau^+$$

$$v(\kappa^2) = (1 + \kappa^2/\alpha^2)^{-1}$$

t_{bg} is the CX part of the non-resonant π-N transition operator. Karapiperis and Kobayashi only include the s-wave part. The coupling f and parameter α are fitted to the π^+-proton p-wave phase-shifts.

The matrix elements of the Δ-N part of the transition operator are

$$\langle f|T_{\Delta N}|i\rangle = \langle f,\text{distorted}|V^\dagger G_{\Delta N} t_{\Delta N} G_{\Delta N} V|i,\text{distorted}\rangle$$

Karapiperis and Kobayashi choose the following zero-range form for the Δ-N interaction, $t_{\Delta N}$:

$$\langle \underline{r}'_\Delta, \underline{r}'_N|t_{\Delta N}|\underline{r}_\Delta, \underline{r}_N\rangle = \delta(\underline{r}'_\Delta - \underline{r}'_N)\delta(\underline{r}_\Delta - \underline{r}_N)\delta(\underline{R}' - \underline{R}) \sum_{S,T} v_{ST} P_S P_T$$

where $\underline{R}$ is the CM coordinate of the Δ-N system and $\underline{r}_\Delta, \underline{r}_N$ are relative coordinates; P_S and P_T are projectors onto the ΔN state with spin S and isospin T; and v_{ST} are complex, energy dependent parameters. Restricting $t_{\Delta N}$ to this form is an oversimplification; more careful treatment may improve quantitative predictions.

The parameters v_{ST} are related to each other. The contribution to the ΔN interaction from S=2 terms is suppressed, so that v_{2T} are small; and the relation between the T=1 and T=2 amplitudes give further restrictions. This leaves effectively one complex parameter for the model, $\delta v \equiv v_{11} - v_{12}$. Note that the sequential part has no free parameters for DCX; the parameters are fixed by elastic scattering.

The propagator $G_{\Delta N}$ includes several terms, such as the kinetic and binding energies of the Δ, the Hamiltonian of the hole nucleus, a correction for Δ-decay to Pauli forbidden states, and a 'spreading potential'. The last

term is a phenomenological term to allow for absorption. This is the only non-microscopic part of the model. The parameters of the spreading potential are allowed to vary from nucleus to nucleus and are energy-dependent. The parameters were fitted to π-nucleus elastic scattering data, and included s-wave repulsive terms.

The distorted initial and final states are obtained using the full Δ-hole elastic optical potential. The initial, intermediate and final nuclear states used were harmonic oscillator states. For ^{18}O and ^{16}O the model of Zuker, Buck and McGrory [57] was used. This has contributions from the $0p_{1/2}$ shell in addition to $0d_{5/2} + 1s_{1/2}$. This allows core nucleons to contribute to DCX; and so the amplitudes for ^{16}O can be calculated with the same methods as ^{18}O.

Karapiperis and Kobayashi have made calculations for the nuclei ^{14}C, ^{16}O and ^{18}O. The calculations include SCX and DCX angular distributions at 50 MeV and 164 MeV, and excitation functions. They obtain reasonable (typically within a factor ~ 2) agreement with much of the data. The main exceptions are

(i) for the ^{18}O angular distribution at 164 MeV for which no value δv gives agreement. ^{16}O data is reproduced by the model, so the model does not account for nuclear structure differences very well.

(ii) The ^{18}O excitation function which fails to predict the cross section peak between 110 MeV and 140 MeV (Fig. 1.5). Instead a reduced cross section is predicted here due to a cancellation between analogue and non-analogue intermediate-state contributions, and between the sequential and ΔN interactions. Karapiperis and Kobayashi feel a more detailed model could easily remove this cancellation.

Fig. 5.5 shows their ^{18}O DCX predictions at 50 MeV with $\delta v = 0.2-2.8i$; this gave the closest prediction. They found the ΔN interaction was not important at 50 MeV, as expected for low energies. So the sequential amplitude can account for 50 MeV DCX data, with no need for exotic mechanisms such as the six-quark cluster.

They find the intermediate analogue-state contributes very little to 50 MeV DCX. This is as expected from SCX data. The main contribution to 50 MeV DCX is from non-analogue intermediate states, and so the s-p cancellation in SCX provides practically no constraint on DCX.

They find pion distortions important. Using plane waves reduces the 0° ^{14}C DCX cross section at 50 MeV by a factor 2.4. Core contributions are also important. Using a simple $(p_{1/2})^2$ model with DCX only on valence neutrons, reduced the cross section by another factor 2.4. One reason for this large factor is that the simple model has no 2^+ state; this state gives a large contribution. SCX is backward peaked, and the 2^+ state is most easily excited by back-scattering a 50 MeV pion. Thus a large contribution from two back scatterings may be responsible for the foward peaking of DCX.

Karapiperis and Kobayashi claim sufficient agreement with data to establish that multiple scattering theory is adequate to describe charge exchange reactions.

6 CONCLUSION

The angular distribution for the DCX reaction to the DIAS for ^{18}O has been measured at 48.3 MeV pion kinetic energy. The 0° differential cross section is 4.7 ± 0.5 μb/sr (by extrapolation). The total (angle integrated) cross section is 16.2 ± 1.2 μb. The angular distribution is forward peaked and very similar to that of ^{14}C.

The forward peaking is not predicted by the simple sequential model. Various proposals have been made for the origin of this forward peaking. These include six-quark cluster effects, short range correlations, and contributions from non-analogue intermediate states.

DCX is expected to provide useful information for π-nucleus models, e.g. on second-order and isotensor terms in the optical potential, and on the Δ-nucleon interaction in the Δ-hole model. It is also expected to give information on nuclear structure such as neutron-proton density differences and short-range correlations.

Low energy pion (~ 50 MeV) DCX reactions are important for understanding the mechanism. The small size of the simple sequential contribution makes other mechanisms easier to study. More data in this energy region is needed to fix parameters and help choose between the various models. The recent measurement of the 50 MeV DCX angular distribution for ^{26}Mg at TRIUMF [23], and the proposals at TRIUMF for measurements on ^{56}Fe, ^{34}S, and the excitation function for ^{18}O from 30 MeV to 80 MeV [24], are important steps towards understanding the DCX mechanism.

BIBLIOGRAPHY

1 R. Baliau, M. Rho, G. Ripka (editors), Nuclear Physics with Heavy Ions and Mesons Vol. II (North Holland Pub. Co. 1977).

2 D.H. Perkins, Introduction to high energy physics 2nd ed. (Addison Wesley 1982).

3 R. Tacik, Ph.D. thesis (University of British Columbia, 1984, unpublished).

4 W. Gyles, Ph.D. thesis (University of British Columbia, 1984, unpublished).

5 K. K. Seth, International Topical Conference on Meson Nuclear Physics, Houston, 1979.

6 G. A. Miller and J. E. Spencer, Ann. Phys. (N.Y.) 100(1976)562.

7 Burman et al., Phys. Rec. C 17(1978)1774.

8 M. J. Leitch et al., Phys. Rev. Lett. 54(1985)1482.

9 S. J. Greene et al., Phys. Rev. C 25(1982)927.

10 F. Irom et al., Phys. Rev. C 28(1983)2565.

11 K. K. Seth et al., Phys. Rev. Lett. 43(1979)1574.

12 S. J. Greene et al., Phys. Rev. C 25(1982)924 and references therein.

13 I. Navon et al., Phys. Rev. Lett. 52(1984)105.

14 A. Doron et al., Phys. Rev. C 26(1982)189.

15 E. R. Siciliano (Unpublished), Results shown in Refs. [8] and [37].

16 G. A. Miller, Phys. Rev. Lett. 53(1984)2008.

17 R. L. Jaffe, Phys. Rev. Lett. 50(1983)228.
C. E. Carlson and T. J. Havens, Phys. Rev. Lett. 51(1983)261.

18 G. Karl, G. A. Miller, and J. Rafelski, Phys. Lett. B 143(1984)326.

19 T. Karapiperis and M. Kobayashi, SIN preprint PR-85-08.

20 T. Karapiperis, Invited talk at the LAMPF workshop on PION DCX, January 10-12, 1985 (in press).

21 T. Karapiperis, M. Kobayashi, and M. Hirata, Phys. Lett. B 144 (1954) 23.

22 B. K. Jennings and N. de Takcasy, Private Communication.

23 R. R. Johnson et al., To be published.

24 A. Altman and T. Anderl, TRIUMF proposals.

25 C. J. Oram et al., NIM 179(1981)95.

26 R. J. Sobie et al., NIM 219(1984)501.

27 W. Gyles et al., Nucl. Phys. A 439(1985)598.

28 A. W. Bennett, MOLLI for use on the VAX (TRIUMF 1983, unpublished).

29 OPDATA User's Guide (TRIUMF, 1985, unpublished).

30 F. M. Rozen, M.Sc. thesis (University of British Columbia, 1984, unpublished).

31 K. L. Brown et al., TRANSPORT - a Computer Program for Designing Partical Beam Transport Systems, CERN report 80-04, 1980.

32 REVMOC User's Guide (TRIUMF, unpublished).

33 B. M. Barnett, Ph.D. thesis (University of British Columbia, 1985, unpublished).

34 W. Anderson, TRIUMF. Private Communication dated 9 January 1985.

35 A. Altman et al., (Submitted to Phys. Rev. Lett.).

36 P. A. Siedl et al., Phys. Rev. C 30(1984)973.

37 M. D. Cooper et al., Phys. Rev. Lett. 52(1984)1100.

38 M. B. Johnson and E. R. Siciliano., Phys. Rev. C 27(1983)1647.

39 L. C. Liu, Phys. Rev. C 27(1983)1611.

40 W. B. Kaufmann, J. C. Jackson, and W. R. Gibbs, Phys. Rev. C 9(1974)1340

41 E. Oset et al., Nucl. Phys. A 408(1983)461.

42 J. R. Taylor, Scattering Theory: the quantum theory on nonrelativistic collisions (Wiley 1972).

43 J. Hüfner, Phys. Rep. C 21(1975)1.

44 K. Stricker, H. McManusand, J. P. Carr, Phys. Rev. C 19(1979)929 and Phys. Rev. C 22(1980)2042.

45 L. C. Liu, Phys. Rev. C 23(1981)814.

46 E. R. Siciliano, talk presented at TRIUMF September 1985.

47 M. B. Johnson, Phys. Rev. C 22(1980)192.

48 M. B. Johnson and E. R. Siciliano, Phys. Rev. C 27(1983)730.

49 P. J. Mulders and A. W. Thomas, J. Phys. G 9(1983)1159.

50 G. A. Miller, Private Communication.

51 B. K. Jennings and N. de Takacsy, Phys. Lett. B 124(1983)302.

52 G. A. Miller, The LAMPF workshop on pion DCX, January 10-12, 1985 (in press).

53 M. Ericson and T. E. O. Ericson, Ann. Phys. 36(1966)323.

54 J. Eisenberg, J. Hüfner and E. J. Moniz, Phys. Lett. B 47(1973)381.

55 J. D. Bjorken and S. D. Drell, Relativistic Quantum Mechanics (McGraw Hill, 1964).

56 See Bibliography in Reference [19].

57 A. P. Zucker, B. Buck and J. B. McGrory, Phys. Rev. Lett. 24(1970)73.

58 L. E. Autonuk et al., SIN preprint PR-83-12, July 1983.